Title: Structure Reveals the Activation Mechanism of the MC4 Receptor to Initiate Satiation Signaling

Authors: Hadar Israeli[1,2,*], Oksana Degtjarik[1,*], Fabrizio Fierro[3], Vidicha Chunilal[4], Amandeep Kaur Gill[4], Nicolas J. Roth[4], Joaquin Botta[4,5], Vadivel Prabahar[1], Yoav Peleg[6], Li F. Chan[4], Danny Ben-Zvi[2,#], Peter J. McCormick[4,#], Masha Y. Niv[3,#], Moran Shalev-Benami[1,#]

Affiliations:

[1]Department of Chemical and Structural Biology, Weizmann Institute of Science, Rehovot 7610001, Israel.

[2]Department of Developmental Biology and Cancer Research, The Institute for Medical Research Israel-Canada, The Hebrew University-Hadassah Medical School, Jerusalem, Israel.

[3]The Faculty of Agriculture, Food and Environment and The Fritz Haber Center for Molecular Dynamics, The Hebrew University, Israel.

[4]Centre for Endocrinology, William Harvey Research Institute, Barts and the London School of Medicine, Queen Mary, University of London, Charterhouse Square, London, United Kingdom.

[5]Current address: Sosei-Heptares, Cambridge, United Kingdom.

[6]Structural Proteomics Unit (SPU), Life Sciences Core Facilities (LSCF), Weizmann Institute of Science, Rehovot 7610001, Israel.

*These authors have contributed equally to this manuscript

[#]Corresponding authors: moransb@weizmann.ac.il; p.mccormick@qmul.ac.uk; masha.niv@mail.huji.ac.il; dannyb@ekmd.huji.ac.il

Abstract:

Obesity is a global epidemic causing morbidity and impaired quality of life. The melanocortin receptor 4 (MC4R) is at the crux of appetite, energy homeostasis, and body-weight control in the central nervous system and is a prime target for anti-obesity drugs. Here, we present the cryo-EM structure of the human MC4R-G_s signaling complex bound to the agonist setmelanotide, a cyclic peptide recently approved for the treatment of obesity. The work reveals the mechanism of MC4R activation, highlighting a molecular switch that initiates satiation signaling. In addition, our findings indicate that Ca^{2+} is required for agonist but not antagonist efficacy. These results fill a gap in understanding MC4R activation and could guide the design of future weight management drugs.

Main text:

Obesity is a global epidemic, with more than 40% of the adult population considered overweight or obese (*1*). Obesity is a major risk factor for chronic diseases, including type 2 diabetes, coronary artery disease, and cancer, and constitutes an important cause of morbidity and impaired quality of life (*2*). Over the years, various weight-loss-targeting drugs have been developed, yet most of these were ultimately removed from the market due to questionable efficacy, lack of target specificity, or severe adverse effects. This highlights the need for a better understanding of the molecular mechanisms governing weight regulation and its related pathologies.

Melanocortin 4 receptor (MC4R) is a member of the melanocortin receptor family (MCRs), a class-A G-protein coupled receptor (GPCR) subgroup consisting of five subtypes (MCR1-5) that mediate multiple physiological effects in humans (*3*). MC4R is abundant throughout the mammalian central nervous system (CNS) and is expressed in particular within the paraventricular nucleus (PVN) of the hypothalamus, a region critical for energy homeostasis (*4–6*). MC4R has been shown to play a key role in modulating satiety in pharmacological and genetic studies in animal models and patients (*7–9*). Loss-of-function mutations in MC4R have been implicated in ~6-8% of early-onset severe obesity cases and are considered the most common form of monogenic obesity (*7*, *10*), while gain-of-function mutations have been linked to low body mass index (BMI) (*9*). Beyond its critical role in the regulation of food intake and energy expenditure, MC4R also functions in other CNS regions with clinical implications in pain sensation, sexual function, anhedonia, and blood pressure regulation (*11–13*).

MC4R is an unusual GPCR as it has both an endogenous agonist and an endogenous antagonist (*14*, *15*). For other GPCRs, with the exception of the close MC4R homolog MC3R (*3*), only endogenous agonists have been described. Specifically, MC4R is activated by the alpha-melanocyte-stimulating hormone (α-MSH), a proopiomelanocortin (POMC) derived peptide, which mediates anorexigenic effects, and is antagonized through binding of the agouti-related peptide (AgRP), which promotes appetite (*14*). A recent crystal structure of MC4R bound to a potent antagonist provided a snapshot of the inactive receptor

conformation (*16*), but the molecular architecture of an active complex with cognate signaling partners remained unknown. We determined the structure of the active human MC4R bound to the cyclic peptide agonist setmelanotide and in complex with the G_s heterotrimer at 3 Å resolution by cryo-EM. Setmelanotide (Imcivree) is a promising weight control drug shown to induce weight loss in patients suffering from POMC deficiency (*17*, *18*), leptin receptor deficiency (*19*) and other forms of severe genetic obesity, and was recently registered by the FDA for the treatment of these conditions (*20–23*).

The molecular architecture of the native MC4R signaling complex

The setmelanotide-MC4R-G_s complex was assembled by supplying agonist to cells co-expressing heterotrimeric G_s and full-length MC4R and was stabilized using the single-chain variable fragment scFv16 (*24*). ScFv16 was originally developed for the stabilization of the G_{i1} heterotrimer and has been used to determine several $G_{i/o}$ and G_q GPCR complex structures (*25–29*). We replaced the αN helix of $G\alpha_s$ (residues 1-38) with that of $G\alpha_{i1}$ (residues 1-31) to enable complex recognition by scFv16 ($G\alpha_{s\text{-}iN}$) (*24*). This strategy yielded a stable G_s heterotrimer that coupled to activated MC4R (**Fig. S1**).

We used single-particle cryo-EM analysis to obtain a three-dimensional reconstruction of the MC4R-G_s complex at a nominal resolution of 3 Å (**Fig. 1, S1-S2** and **Tables S1-S2**). The map revealed the architectures of all complex components, as well as the mode of receptor association with the G_s heterotrimer and the orientation of setmelanotide within the orthosteric binding pocket (**Fig. 1C-D**). Most notably, MC4R differs from previously reported class-A GPCR–G-protein complexes in the extracellular region, which is relatively open, containing an exposed cavity of 1082 $Å^3$ (**Fig. 2B-C** and **S3A**). This feature can be attributed to a short extracellular loop 2 (ECL2) that lacks secondary structural elements compared with other class-A members (**Fig. S3B**) (*30*). As noted previously (*16*), MC4R lacks a disulfide found in other class-A GPCRs connecting ECL2 with trans-membrane helix 3 (TM3) (*31*). Instead, the MC4R extracellular region has two other disulfides, which link the N-terminus to TM7, and ECL3 to TM6, both

of which are clearly visualized in our EM density ($C40^{N\text{-}term}$-$C279^{7.30}$ and $C271^{6.61}$-$C277^{ECL3}$; superscript numbers correspond to the Ballesteros-Weinstein nomenclature; **Fig. S2G**). Overall, our structure enables the analysis of the full-length, active MC4R coupled with its cognate cellular effectors and supplies residue-resolution information on the main signaling pathway leading to satiety.

Description of setmelanotide in the MC4R binding pocket

Setmelanotide is a potent mimetic of α-MSH, the endogenous hormone agonist that acts on MC4R to signal satiety and increase energy expenditure (**Fig. 2A**). Unlike α-MSH, setmelanotide is linked by a disulfide bond between cysteines near its termini. Setmelanotide contains the highly conserved HFRW motif that is shared between all POMC-derived peptides and contributes directly to the activation of receptors of the MCR family (*32*). However, the phenylalanine in setmelanotide is in the D configuration, whereas it is in the L conformation in α-MSH (**Fig. 2A**).

In the cryo-EM structure, setmelanotide engages MC4R through extensive electrostatic and hydrophobic interactions with residues in the transmembrane domain (**Fig. 3A**). These interactions are mostly attributed to the HFRW motif and include hydrogen bonds with S188, π-π stacking interaction with F51, C–H···O contacts (*33*) with Y268 and F284, and hydrophobic contacts with T101, I129, L133, I185, I194 and F261 (**Fig. 3A**). Most of these residues are highly conserved among the MCR family and account for the cross reactivity with POMC-derived peptides. Interactions outside the HFRW motif include contacts between Cys_8 in setmelanotide and Y268, and F284 in the receptor, only the last of which is conserved in members of the MCR family (**Fig. 3B**, **Fig. S4**). Additional contacts are from Arg_1 and Ala_3 to D122 and I104, respectively, both of which are conserved in MCR family members. Arg_1 in setmelanotide substitutes for a serine in α-MSH and likely contributes to the elevated potency of the drug compared with the endogenous hormone (**Fig. 2A**,**D**).

A notable feature of setmelanotide binding is a Ca^{2+} ion coordinated by both the agonist and the receptor. A Ca^{2+} ion was observed in a similar position in the complex of MC4R with the synthetic antagonist

SHU9119 (**Fig. 3C**, (*16*)). In both structures, the receptor contributes the side chains of the acidic residues ($D122^{3.25}$, $D126^{3.29}$ and $E100^{2.60}$) to Ca^{2+} coordination, and both setmelanotide and SHU9119 have a direct interaction to the ion using the D-Phe_5 backbone oxygen (D-naphthyl alanine, D-Nal_4 in SHU9119, **Fig. 3C**). One difference in the coordination of the Ca^{2+} between the antagonist and agonist structures is that SHU9119 contributes the backbone carbonyl of Asp_2 in a backbone-ligand interaction, whereas setmelanotide uses a water-mediated interaction between the backbone carbonyl of D-Ala_3 and the ion (**Fig. 3C**, **S2F**). Molecular dynamics simulations suggest that the backbone carbonyl of Cys_2 may alternate with the backbone carbonyl of D-Ala_3 in creating the water-mediated interaction (**Fig. S5A-B**).

Ca^{+2} functions as a cofactor required for receptor activation but not inhibition

Molecular dynamics simulations support Ca^{2+} binding by MC4R even in the absence of a ligand, suggesting that Ca^{2+} may have a ligand-independent role or may prime the pocket for ligand binding (**Fig. 3D** and **Fig. S5C-D**). While the simulations suggest that Ca^{2+} does not depend on other ligands for binding, MC4R agonists require Ca^{2+} to achieve full efficacy. The EC_{50} for both α-MSH and setmelanotide decreased by about two orders of magnitude in the presence of physiological Ca^{2+} concentrations (1 mM) in our cellular assays (**Fig. 4A-B and S6**). Indeed, an estimation of a K_B for Ca^{2+} (0.06μM, **Fig. S6M**) supports Ca^{2+} binding at physiologic levels to MC4R. Notably, other divalent ions did not have similar effects, nor did we detect allosteric effects on Ca^{2+} binding caused by the presence of other ions (**Fig. S6A-J**). These results are in accordance with several previous reports that α-MSH as well as synthetic agonists depend on the presence of Ca^{2+} for signaling, with no significant change in response to other ions (*16*, *34*). We also found that the non-peptide synthetic MC4R agonist THIQ, depends on Ca^{2+} for enhanced activity and binding (**Fig. S7**).

In contrast, we found that physiological Ca^{2+} concentrations do not contribute to inverse-agonist activity of SHU9119, nor to AgRP-induced antagonistic activity. Signaling assays revealed that physiological Ca^{2+} concentrations do not significantly impact the ability of SHU9119 to compete with α-MSH, and that AgRP

activity is in fact hampered by the presence of Ca^{2+} (**Fig. 4C-D**). This suggests that Ca^{2+} plays a role in modulating receptor susceptibility to endogenous agonists and antagonists.

Notably, one of the residues that was found to coordinate Ca^{+2} positioning within the binding pocket and modulate ligand accommodation in the receptor, $D122^{3.25}$, corresponds to a conserved cysteine residue in other class-A members, which composes a disulfide bridge missing in MCRs (**Fig. S8A-C**). These data highlight the possibility that Ca^{+2} serves as a surrogate to the function of the bridge and contributes to the structural integrity of the canonical binding pocket. Given the opposite effect of Ca^{2+} on the endogenous agonist and antagonist, we suggest that Ca^{2+} can provide MC4R sufficient flexibility to modulate the binding pocket to differentially accommodate agonists and antagonists.

Mutation of residues involved in Ca^{2+} coordination reduces receptor activation

Mutational studies were conducted to further explore the function of Ca^{2+} coordination in receptor activity and to assess the implications for human disease. Two of the Ca^{2+} coordinating residues, D122N and D126Y, are naturally occurring mutations associated with obesity (*18*, *35*). An E100A mutation was introduced to probe the function of the third Ca^{2+} coordinating side chain. The D122N mutant displayed a two-log increase in EC_{50} and ~50% decrease in efficacy for α-MSH and setmelanotide under physiological Ca^{2+} concentrations. For the E100A mutant, the impairment was not the same for the natural and artificial agonists. While α-MSH signaling was almost completely abolished by the E100A mutation, setmelanotide was still able to signal, but at half maximum and with a two-log increase in EC_{50} (**Fig. 4E-F**). The D126Y mutant resulted in the complete abolishment of receptor function. The more pronounced effect of the D126 substitution can be explained by the fact that D122 and E100 each contribute a single bond to Ca^{2+} coordination, whereas D126 contributes two (**Fig. 3C**). Both the D122N and E100A mutants remained dependent on Ca^{2+} for signaling for both setmelanotide and α-MSH, suggesting that altering the aspartates at these positions did not eliminate Ca^{2+} coordination (**Fig. S8E-F**). Flow cytometry analysis indicated similar profiles of surface expression levels for wild-type and mutant receptors, indicating that the observed

activity changes were not due to poor cell surface availability (**Fig. S8D**). These results are in agreement with previously reported work in which mutations at positions 122 and 126 in MC4R resulted in impaired ligand binding properties (*18*, *35–38*). The differential activation profile of the D122N variant by setmelanotide compared with α-MSH, highlights setmelanotide as a potential therapeutic path for individuals harboring a D122N mutation. Discussion of common mutations in MC4R is further provided in **Fig. S9**.

Identification of a mechanical activation switch in MC4R

Comparing the inactive and active states of MC4R, the outward displacement of TM6 is clearly evident (**Fig. 5A** and **S3C**). This structural rearrangement is a hallmark of GPCR activation, allowing the C-terminal α5 helix of the $G\alpha_s$ subunit to engage the receptor core and initiate signaling. In MC4R, binding of the agonist setmelanotide partly resembles the binding of the antagonist SHU9119 (*16*) (**Fig. 2-3**), raising the question of how the structural change and GPCR activation are induced selectively by the agonist. A noticeable difference between the binding modes of the antagonist and the agonist is that the D-Nal_4 group of SHU9119, which is bulkier than the D-Phe_5 in setmelanotide, penetrates the binding pocket more deeply and interacts with $L133^{3.36}$ (**Fig. 2B-C**, **5B**). $L133^{3.36}$ is a key modulator in class-A GPCR activation, as it directly interacts with $W258^{6.48}$, which plays a crucial role in TM6 displacement during receptor transition to the active state (*31*). In the inactive state, $L133^{3.36}$ engages the aromatic face of $W258^{6.48}$, with the two methyl groups facing the π-electrons and maintaining CH-π contacts (**Fig. 5B**). In the active conformation, $L133^{3.36}$ is oriented, with the two methyl groups facing away from $W258^{6.48}$. As a result, $W258^{6.48}$ is free to accommodate an alternate state that allows for the conformational rearrangement of TM6 required for G-protein coupling (**Fig. 5A-B**). This conformational change resembles the classic toggle switch in other GPCRs, where in the inactive state $F^{3.36}$ stacks upon $W^{6.48}$ to maintain the inactive receptor, whereas in the active conformation $F^{3.36}$ rotates and allows the release of $W^{6.48}$ (e.g., CB1R (*26*, *39*), CB2R (*40*), and CCR5 (*41*), **Fig. 5C**). Comparison between the agonist- and antagonist- bound structures suggests that while

SHU9119 sterically hinders the displacement of L133$^{3.36}$ toward the active state, the phenyl residue in setmelanotide stabilizes the active state conformation (**Fig. 5B**).

A challenge in targeting MC4R is to avoid undesired side effects due to cross reactivity with other members of the MCR family (e.g. MC3R and MC1R). Thus, identifying distinct features in the activation mechanism of MC4R is important. MC1R is a close homolog of MC4R, and cross-reactivity with MC1R is often observed when agonists and antagonists designed for MC4R are used clinically (*18*, *22*). Further evidence can be seen in patients treated with afamelanotide, an MC1R agonist used for the treatment of erythropoietic protoporphyria, these patients often suffer from decreased appetite due to cross reactivity with MC4R (*42*). A puzzling observation is that MC4R antagonists such as SHU9119 act as agonists for MC1R (*43*). Residues in the orthosteric binding pocket of MC4R and MC1R are almost identical, but L133$^{3.36}$ of the MC4R activation switch is replaced by a methionine, M128$^{3.36}$, in MC1R (**Fig. S4**). We introduced an L133M mutation into MC4R and confirmed that SHU9119 acts as an agonist for this mutant (**Fig. S8G-I**). In contrast, we found that AgRP did not activate the mutant receptor, suggesting differences in the binding mode for the endogenous antagonist compared with the synthetic derivative (**Fig. S8G**). Comparing the MC4R structure to structures harboring a 3.36 methionine (e.g. the μ-opioid receptor - MOR1), shows that the rotameric state of L133$^{3.36}$ in an inactive MC4R overlaps with the active state of M151$^{3.36}$ in MOR1 (**Fig. S8J**). Furthermore, superposition of the structure of MC4R bound to SHU9119 with an inactive structure of MOR1 indicates a clash between the naphthyl group in SHU9119 and M151$^{3.36}$ (**Fig. S8K**). These observations suggest why SHU9119 contributes to agonistic activity in the mutant. These experiments also demonstrate the potential for a selectivity window to reduce the cross reactivity with MC1R that contains a methionine at position 3.36. A full analysis of conserved and synonymous residues in the binding pocket of MCR family members is provided in **Fig. S4**.

Exploring MC4R canonical and non-canonical signaling pathways

The conventional $G\alpha_s$ signaling of MC4R is crucial in inducing anorexogenic signaling in the hypothalamus to result in negative energy balance (*44–46*). However, MC4R can activate other signaling mediators to trigger downstream signaling effects. These include coupling to $G\alpha_i$, $G\alpha_q$, and $G\alpha_{15}$, interaction with β-arrestins (*47*, *48*), and through G-protein independent coupling to the inwardly rectifying potassium channel Kir7.1 (*49*). Our work presents the structural mechanistic properties of MC4R activation by setmelanotide and captures the MC4R-G_s bound state that allows for the delineation of the coupling interface. The MC4R-$G\alpha_s$ interface is mostly composed of interactions between residues in TM3, TM5 and TM6 at the receptor and the C-terminal helix (α5 helix) of $G\alpha_s$ (**Fig. 6A** and **S10**). These interactions also include a class-A conserved π-cation stacking between $Y370^{H5.23}$ in G_s, and $R147^{3.50}$ in MC4R, where $R^{3.50}$ composes part of the DRY motif that plays an important role in G-protein coupling (*50–54*). All residues in MC4R that are involved in G_s interactions are strictly conserved among all MCR family members, reflecting their shared coupling to G_s (**Fig. S4A**) (*55*). In addition, MC4R mutations in residues involved in G_s recruitment have been associated with impaired signaling through the G_s pathway and have also been identified in obese individuals (*56*, *57*). Notable examples are A219V and T150I, which demonstrate impaired cAMP production without change in binding affinity to α-MSH compared with the wild-type receptor (*9*, *35*, *58–61*). $A219^{5.65}$ is close to the tip of $G\alpha_s$ helix α5. Substitution of Ala with a bulkier Val might create a clash that would disturb MC4R-$G\alpha_s$ binding. Residues that interact with $A219^{5.65}$ ($L367^{H5.20}$, $L372^{H5.25}$, and $L373^{H5.26}$) are also conserved in G_q and G_{15}, both reported to bind MC4R (*47*, *62*), thus mutations at this position, might also interfere with signaling through alternative pathways for this receptor. $T150^{3.53}$ is located at the tip of TM3 and contributes two hydrogen bonds to the binding interface through direct interactions with H366 and Y370. Substitution of Thr by hydrophobic Ile would abolish one of the hydrogen bonds, thus impairing recruitment of the Gα subunit.

A recent genetic variant study showed that mutations in MC4R observed in patients with low BMI were associated with MC4R gain-of-function through biased β-arrestin 2 recruitment to the receptor. These studies highlight the importance of targeting preferred pathways by drugs to treat obesity (*9*). Analysis of mutations associated with gain-of-function or loss of function of MC4R is provided in **Fig. S9**. Comparing setmelanotide and α-MSH ability to recruit $G\alpha_s$ or β-arrestin 2, we saw no bias towards these two pathways (**Fig. 6B-C**). Thus our studies suggest that for the wild-type receptor, both setmelanotide and α-MSH will act similarly to activate these pathways.

In summary, this work provides a major leap in our understanding of the molecular basis of MC4R activation and inhibition, ligand specificity, and the contribution of genetic variations to MC4R-related pathologies. Looking forward, this work will set the stage for future efforts to develop novel therapeutic strategies to fight obesity and possibly other weight-regulation disorders.

References

1. Obesity and overweight. *World Heal. Organ.*, (available at https://www.who.int/news-room/fact-sheets/detail/obesity-and-overweight).
2. M. Blüher, Obesity: global epidemiology and pathogenesis. *Nat. Rev. Endocrinol.* **15** (2019), pp. 288–298.
3. K. L. J. Ellacott, R. D. Cone, The central melanocortin system and the integration of short- and long-term regulators of energy homeostasis. *Recent Prog. Horm. Res.* **59**, 395–408 (2004).
4. K. G. Mountjoy, M. T. Mortrud, M. J. Low, R. B. Simerly, R. D. Cone, Localization of the melanocortin-4 receptor (MC4-R) in neuroendocrine and autonomic control circuits in the brain. *Mol. Endocrinol.* **8**, 1298–1308 (1994).
5. J. Rossi, N. Balthasar, D. Olson, M. Scott, E. Berglund, C. E. Lee, M. J. Choi, D. Lauzon, B. B. Lowell, J. K. Elmquist, Melanocortin-4 receptors expressed by cholinergic neurons regulate energy balance and glucose homeostasis. *Cell Metab.* **13**, 195–204 (2011).
6. B. P. Shah, L. Vong, D. P. Olson, S. Koda, M. J. Krashes, C. Ye, Z. Yang, P. M. Fuller, J. K.

Elmquist, B. B. Lowell, MC4R-expressing glutamatergic neurons in the paraventricular hypothalamus regulate feeding and are synaptically connected to the parabrachial nucleus. *Proc. Natl. Acad. Sci. U. S. A.* **111**, 13193–13198 (2014).

7. I. S. Farooqi, J. M. Keogh, G. S. H. Yeo, E. J. Lank, T. Cheetham, S. O'Rahilly, Clinical Spectrum of Obesity and Mutations in the Melanocortin 4 Receptor Gene. *N. Engl. J. Med.* **348**, 1085–1095 (2003).

8. A. S. Garfield, C. Li, J. C. Madara, B. P. Shah, E. Webber, J. S. Steger, J. N. Campbell, O. Gavrilova, C. E. Lee, D. P. Olson, J. K. Elmquist, B. A. Tannous, M. J. Krashes, B. B. Lowell, A neural basis for melanocortin-4 receptor-regulated appetite. *Nat. Neurosci.* **18**, 863–871 (2015).

9. L. A. Lotta, J. Mokrosiński, E. Mendes de Oliveira, C. Li, S. J. Sharp, J. Luan, B. Brouwers, V. Ayinampudi, N. Bowker, N. Kerrison, V. Kaimakis, D. Hoult, I. D. Stewart, E. Wheeler, F. R. Day, J. R. B. Perry, C. Langenberg, N. J. Wareham, I. S. Farooqi, Human Gain-of-Function MC4R Variants Show Signaling Bias and Protect against Obesity. *Cell*. **177**, 597–607 (2019).

10. K. K. Alharbi, E. Spanakis, K. Tan, M. J. Smith, M. A. Aldahmesh, S. D. O'Dell, A. A. Sayer, D. A. Lawlor, S. Ebrahim, G. Davey Smith, S. O'Rahilly, S. Farooqi, C. Cooper, D. I. W. Phillips, I. N. M. Day, Prevalence and functionality of paucimorphic and private *MC4R* mutations in a large, unselected European British population, scanned by meltMADGE. *Hum. Mutat.* **28**, 294–302 (2007).

11. L. H. T. Van der Ploeg, W. J. Martin, A. D. Howard, R. P. Nargund, C. P. Austin, X. Guan, J. Drisko, D. Cashen, I. Sebhat, A. A. Patchett, D. J. Figueroa, A. G. DiLella, B. M. Connolly, D. H. Weinberg, C. P. Tan, O. C. Palyha, S. S. Pong, T. MacNeil, C. Rosenblum, A. Vongs, R. Tang, H. Yu, A. W. Sailer, T. M. Fong, C. Huang, M. R. Tota, R. S. Chang, R. Stearns, C. Tamvakopoulos, G. Christ, D. L. Drazen, B. D. Spar, R. J. Nelson, D. E. MacIntyre, A role for the melanocortin 4 receptor in sexual function. *Proc. Natl. Acad. Sci. U. S. A.* **99**, 11381–11386 (2002).

12. M. Beltramo, M. Campanella, G. Tarozzo, S. Fredduzzi, L. Corradini, A. Forlani, R. Bertorelli, A.

Reggiani, Gene expression profiling of melanocortin system in neuropathic rats supports a role in nociception. *Mol. Brain Res.* **118**, 111–118 (2003).

13. B. K. Lim, K. W. Huang, B. A. Grueter, P. E. Rothwell, R. C. Malenka, Anhedonia requires MC4R-mediated synaptic adaptations in nucleus accumbens. *Nature*. **487**, 183–189 (2012).

14. M. M. Ollmann, B. D. Wilson, Y. K. Yang, J. A. Kerns, Y. Chen, I. Gantz, G. S. Barsh, Antagonism of Central Melanocortin receptors in vitro and in vivo by agouti-related protein. *Science.* **278**, 135–138 (1997).

15. I. Suzuki, A. Tada, M. M. Ollmann, G. S. Barsh, S. Im, M. L. Lamoreux, V. J. Hearing, J. J. Nordlund, Z. A. Abdel-Malek, Agouti signaling protein inhibits melanogenesis and the response of human melanocytes to α-melanotropin. *J. Invest. Dermatol.* **108**, 838–842 (1997).

16. J. Yu, L. E. Gimenez, C. C. Hernandez, Y. Wu, A. H. Wein, G. W. Han, K. McClary, S. R. Mittal, K. Burdsall, B. Stauch, L. Wu, S. N. Stevens, A. Peisley, S. Y. Williams, V. Chen, G. L. Millhauser, S. Zhao, R. D. Cone, R. C. Stevens, Determination of the melanocortin-4 receptor structure identifies Ca2+ as a cofactor for ligand binding. *Science.* **368**, 428–433 (2020).

17. P. Kühnen, K. Clément, S. Wiegand, O. Blankenstein, K. Gottesdiener, L. L. Martini, K. Mai, U. Blume-Peytavi, A. Grüters, H. Krude, Proopiomelanocortin Deficiency Treated with a Melanocortin-4 Receptor Agonist. *N. Engl. J. Med.* **375**, 240–246 (2016).

18. T. H. Collet, B. Dubern, J. Mokrosinski, H. Connors, J. M. Keogh, E. Mendes de Oliveira, E. Henning, C. Poitou-Bernert, J. M. Oppert, P. Tounian, F. Marchelli, R. Alili, J. Le Beyec, D. Pépin, J. M. Lacorte, A. Gottesdiener, R. Bounds, S. Sharma, C. Folster, B. Henderson, S. O'Rahilly, E. Stoner, K. Gottesdiener, B. L. Panaro, R. D. Cone, K. Clément, I. S. Farooqi, L. H. T. Van der Ploeg, Evaluation of a melanocortin-4 receptor (MC4R) agonist (Setmelanotide) in MC4R deficiency. *Mol. Metab.* **6**, 1321–1329 (2017).

19. K. Clément, H. Biebermann, I. S. Farooqi, L. Van Der Ploeg, B. Wolters, C. Poitou, L. Puder, F. Fiedorek, K. Gottesdiener, G. Kleinau, N. Heyder, P. Scheerer, U. Blume-Peytavi, I. Jahnke, S.

Sharma, J. Mokrosinski, S. Wiegand, A. Müller, K. Weiß, K. Mai, J. Spranger, A. Grüters, O. Blankenstein, H. Krude, P. Kühnen, MC4R agonism promotes durable weight loss in patients with leptin receptor deficiency. *Nat. Med.* **24**, 551–555 (2018).

20. K. Clément, E. Van Den Akker, J. Argente, A. Bahm, W. K. Chung, H. Connors, K. De Waele, I. S. Farooqi, Efficacy and safety of setmelanotide , an MC4R agonist , in individuals with severe obesity due to LEPR or POMC. *Lancet Diabetes Endocrino*. **8**, 960–970 (2020).

21. FDA approves first treatment for weight management for people with certain rare genetic conditions (2020), (available at https://www.fda.gov/drugs/drug-safety-and-availability/fda-approves-first-treatment-weight-management-people-certain-rare-genetic-conditions).

22. R. Haws, S. Brady, E. Davis, K. Fletty, G. Yuan, G. Gordon, M. Stewart, J. Yanovski, Effect of setmelanotide, a melanocortin-4 receptor agonist, on obesity in Bardet-Biedl syndrome. *Diabetes, Obes. Metab.* (2020), doi:10.1111/dom.14133.

23. A. Markham, Setmelanotide: First Approval. *Drugs*, 1–7 (2021).

24. S. Maeda, A. Koehl, H. Matile, H. Hu, D. Hilger, G. F. X. Schertler, A. Manglik, G. Skiniotis, R. J. P. Dawson, B. K. Kobilka, Development of an antibody fragment that stabilizes GPCR/G-protein complexes. *Nat. Commun.* **9**, 1–9 (2018).

25. A. Koehl, H. Hu, S. Maeda, Y. Zhang, Q. Qu, J. M. Paggi, N. R. Latorraca, D. Hilger, R. Dawson, H. Matile, G. F. X. Schertler, S. Granier, W. I. Weis, R. O. Dror, A. Manglik, G. Skiniotis, B. K. Kobilka, Structure of the μ-opioid receptor-Gi protein complex. *Nature*. **558**, 547–552 (2018).

26. K. Krishna Kumar, M. Shalev-Benami, M. J. Robertson, H. Hu, S. D. Banister, S. A. Hollingsworth, N. R. Latorraca, H. E. Kato, D. Hilger, S. Maeda, W. I. Weis, D. L. Farrens, R. O. Dror, S. V. Malhotra, B. K. Kobilka, G. Skiniotis, Structure of a Signaling Cannabinoid Receptor 1-G Protein Complex. *Cell*. **176**, 448-458.e12 (2019).

27. S. Maeda, Q. Qu, M. J. Robertson, G. Skiniotis, B. K. Kobilka, Structures of the M1 and M2 muscarinic acetylcholine receptor/G-protein complexes. *Science.* **364**, 552–557 (2019).

28. K. Kim, T. Che, O. Panova, J. F. DiBerto, J. Lyu, B. E. Krumm, D. Wacker, M. J. Robertson, A. B. Seven, D. E. Nichols, B. K. Shoichet, G. Skiniotis, B. L. Roth, Structure of a Hallucinogen-Activated Gq-Coupled 5-HT2A Serotonin Receptor. *Cell*. **182**, 1574-1588.e19 (2020).

29. J. Yin, K. Y. M. Chen, M. J. Clark, M. Hijazi, P. Kumari, X. chen Bai, R. K. Sunahara, P. Barth, D. M. Rosenbaum, Structure of a D2 dopamine receptor–G-protein complex in a lipid membrane. *Nature*. **584**, 125–129 (2020).

30. B. Holst, T. W. Schwartz, Molecular Mechanism of Agonism and Inverse Agonism in the Melanocortin Receptors: Zn+2 as a Structural and Functional Probe. *Ann. N. Y. Acad. Sci*. **994**, 1–11 (2003).

31. A. J. Venkatakrishnan, X. Deupi, G. Lebon, C. G. Tate, G. F. Schertler, M. Madan Babu, Molecular signatures of G-protein-coupled receptors. *Nature*. **494**, 185–194 (2013).

32. J. P. L. Gonçalves, D. Palmer, M. Meldal, MC4R Agonists: Structural Overview on Antiobesity Therapeutics. *Trends Pharmacol. Sci.* **39**, 402–423 (2018).

33. L. Jiang, L. Lai, CH···O hydrogen bonds at protein-protein interfaces. *J. Biol. Chem.* **277**, 37732–37740 (2002).

34. R. Link, S. Veiksina, M. J. Tahk, T. Laasfeld, P. Paiste, S. Kopanchuk, A. Rinken, The constitutive activity of melanocortin-4 receptors in cAMP pathway is allosterically modulated by zinc and copper ions. *J. Neurochem.* **153**, 346–361 (2020).

35. F. Stutzmann, K. Tan, V. Vatin, C. Dina, B. Jouret, J. Tichet, B. Balkau, N. Potoczna, F. Horber, S. O'Rahilly, I. S. Farooqi, P. Froguel, D. Meyre, Prevalence of melanocortin-4 receptor deficiency in europeans and their age-dependent penetrance in multigenerational pedigrees. *Diabetes*. **57**, 2511–2518 (2008).

36. Z. Q. Wang, Y. X. Tao, Functional studies on twenty novel naturally occurring melanocortin-4 receptor mutations. *Biochim. Biophys. Acta - Mol. Basis Dis.* **1812**, 1190–1199 (2011).

37. B. A. Fleck, C. Chen, W. Yang, R. Huntley, S. Markison, S. A. Nickolls, A. C. Foster, S. R. J. Hoare,

Molecular interactions of nonpeptide agonists and antagonists with the melanocortin-4 receptor. *Biochemistry*. **44**, 14494–14508 (2005).

38. Y. Yang, T. M. Fong, C. J. Dickinson, C. Mao, J. Y. Li, M. R. Tota, R. Mosley, L. H. T. Van der Ploeg, I. Gantz, Molecular determinants of ligand binding to the human melanocortin-4 receptor. *Biochemistry*. **39**, 14900–14911 (2000).

39. S. D. McAllister, D. P. Hurst, J. Barnett-Norris, D. Lynch, P. H. Reggio, M. E. Abood, Structural mimicry in class A G protein-coupled receptor rotamer toggle switches: The importance of the F3.36(201)/W6.48(357) interaction in cannabinoid CB1 receptor activation. *J. Biol. Chem.* **279**, 48024–48037 (2004).

40. X. Li, T. Hua, K. Vemuri, J. H. Ho, Y. Wu, L. Wu, P. Popov, O. Benchama, N. Zvonok, K. Locke, L. Qu, G. W. Han, M. R. Iyer, R. Cinar, N. J. Coffey, J. Wang, M. Wu, V. Katritch, S. Zhao, G. Kunos, L. M. Bohn, A. Makriyannis, R. C. Stevens, Z. J. Liu, Crystal Structure of the Human Cannabinoid Receptor CB2. *Cell*. **176**, 459-467.e13 (2019).

41. Q. Tan, Y. Zhu, J. Li, Z. Chen, Structure of the CCR5 chemokine receptor - HIV entry inhibitor Maraviroc complex. *Science.* **341**, 1387–1390 (2013).

42. E. I. Minder, J. Barman-Aksoezen, X. Schneider-Yin, Pharmacokinetics and Pharmacodynamics of Afamelanotide and its Clinical Use in Treating Dermatologic Disorders. *Clin. Pharmacokinet.* **56**, 815–823 (2017).

43. Y. Yang, M. Chen, Y. Lai, I. Gantz, K. E. Georgeson, C. M. Harmon, Molecular determinants of human melanocortin-4 receptor responsible for antagonist SHU9119 selective activity. *J. Biol. Chem.* **277**, 20328–20335 (2002).

44. Y. Minokoshi, T. Alquier, H. Furukawa, Y. B. Kim, A. Lee, B. Xue, J. Mu, F. Foufelle, P. Ferré, M. J. Birnbaum, B. J. Stuck, B. B. Kahn, AMP-kinase regulates food intake by responding to hormonal and nutrient signals in the hypothalamus. *Nature*. **428**, 569–574 (2004).

45. K. G. Mountjoy, L. S. Robbins, M. T. Mortrud, R. D. Cone, The cloning of a family of genes that

encode the melanocortin receptors. *Science.* **257**, 1248–1251 (1992).

46. I. Gantz, H. Miwa, Y. Konda, Y. Shimoto, T. Tashiro, S. J. Watson, J. DelValle, T. Yamada, Molecular cloning, expression, and gene localization of a fourth melanocortin receptor. *J. Biol. Chem.* **268**, 15174–15179 (1993).

47. C. Avet, A. Mancini, B. Breton, C. Le Gouill, A. Hauser, C. Normand, H. Kobayashi, F. Gross, M. Hogue, V. Lukasheva, S. Morissette, E. Fauman, J.-P. Fortin, S. Schann, X. Leroy, D. E. Gloriam, M. Bouvier, Selectivity Landscape of 100 Therapeutically Relevant GPCR Profiled by an Effector Translocation-Based BRET Platform. *SSRN Electron. J.*, 1–41 (2020).

48. A. Inoue, F. Raimondi, F. M. N. Kadji, G. Singh, T. Kishi, A. Uwamizu, Y. Ono, Y. Shinjo, S. Ishida, N. Arang, K. Kawakami, J. S. Gutkind, J. Aoki, R. B. Russell, Illuminating G-Protein-Coupling Selectivity of GPCRs. *Cell*. **177**, 1933-1947.e25 (2019).

49. M. Ghamari-Langroudi, G. J. Digby, J. A. Sebag, G. L. Millhauser, R. Palomino, R. Matthews, T. Gillyard, B. L. Panaro, I. R. Tough, H. M. Cox, J. S. Denton, R. D. Cone, G. J. Digby, R. D. Cone, T. Gillyard, J. A. Sebag, M. Ghamari-Langroudi, I. R. Tough, H. M. Cox, R. Palomino, G. L. Millhauser, R. Matthews, B. L. Panaro, G-protein-independent coupling of MC4R to Kir7.1 in hypothalamic neurons. *Nature*. **520**, 94–98 (2015).

50. J. Ballesteros, S. Kitanovic, F. Guarnieri, P. Davies, B. J. Fromme, K. Konvicka, L. Chi, R. P. Millar, J. S. Davidson, H. Weinstein, S. C. Sealfon, Functional microdomains in G-protein-coupled receptors: The conserved arginine-cage motif in the gonadotropin-releasing hormone receptor. *J. Biol. Chem.* **273**, 10445–10453 (1998).

51. B. Carpenter, R. Nehmé, T. Warne, A. G. W. Leslie, C. G. Tate, Structure of the adenosine A 2A receptor bound to an engineered G protein. *Nature*. **536**, 104–107 (2016).

52. X. Lin, M. Li, N. Wang, Y. Wu, Z. Luo, S. Guo, G. W. Han, S. Li, Y. Yue, X. Wei, X. Xie, Y. Chen, S. Zhao, J. Wu, M. Lei, F. Xu, Structural basis of ligand recognition and self-activation of orphan GPR52. *Nature*. **579**, 152–157 (2020).

53. G. E. Rovati, V. Capra, R. R. Neubig, The highly conserved DRY motif of class A G protein-coupled receptors: Beyond the ground state. *Mol. Pharmacol.* **71**, 959–964 (2007).

54. L.-K. Yang, Y.-X. Tao, Alanine Scanning Mutagenesis of the DRYxxI Motif and Intracellular Loop 2 of Human Melanocortin-4 Receptor. *Int. J. Mol. Sci.* **21**, 7611 (2020).

55. A. R. Rodrigues, H. Almeida, A. M. Gouveia, Intracellular signaling mechanisms of the melanocortin receptors: Current state of the art. *Cell. Mol. Life Sci.* **72**, 1331–1345 (2015).

56. Z. C. Fan, Y. X. Tao, Functional characterization and pharmacological rescue of melanocortin-4 receptor mutations identified from obese patients. *J. Cell. Mol. Med.* **13**, 3268–3282 (2009).

57. Y. X. Tao, D. L. Segaloff, Functional analyses of melanocortin-4 receptor mutations identified from patients with binge eating disorder and nonobese or obese subjects. *J. Clin. Endocrinol. Metab.* **90**, 5632–5638 (2005).

58. L. H. Larsen, S. M. Echwald, T. I. A. Sørensen, T. Andersen, B. S. Wulff, O. Pedersen, Prevalence of mutations and functional analyses of melanocortin 4 receptor variants identified among 750 men with juvenile-onset obesity. *J. Clin. Endocrinol. Metab.* **90**, 219–224 (2005).

59. Z. Xiang, B. Proneth, M. L. Dirain, S. A. Litherland, C. Haskell-Luevano, Pharmacological characterization of 30 human melanocortin-4 receptor polymorphisms with the endogenous proopiomelanocortin-derived agonists, synthetic agonists, and the endogenous agouti-related protein antagonist. *Biochemistry*. **49**, 4583–4600 (2010).

60. Z. Xiang, S. A. Litherland, N. B. Sorensen, B. Proneth, M. S. Wood, A. M. Shaw, W. J. Millard, C. Haskell-Luevano, Pharmacological characterization of 40 human melanocortin-4 receptor polymorphisms with the endogenous proopiomelanocortin-derived agonists and the agouti-related protein (AGRP) antagonist. *Biochemistry*. **45**, 7277–7288 (2006).

61. C. Lubrano-Berthelier, B. Dubern, J. M. Lacorte, F. Picard, A. Shapiro, S. Zhang, S. Bertrais, S. Hercberg, A. Basdevant, K. Clement, C. Vaisse, Melanocortin 4 receptor mutations in a large cohort of severely obese adults: Prevalence, functional classification, genotype-phenotype relationship, and

lack of association with binge eating. *J. Clin. Endocrinol. Metab.* **91**, 1811–1818 (2006).

62. Y. Q. Li, Y. Shrestha, M. Pandey, M. Chen, A. Kablan, O. Gavrilova, S. Offermanns, L. S. Weinstein, Gq/11 α and Gs α mediate distinct physiological responses to central melanocortins. *J. Clin. Invest.* **126**, 40–49 (2016).

63. T. Unger, Y. Jacobovitch, A. Dantes, R. Bernheim, Y. Peleg, Applications of the Restriction Free (RF) cloning procedure for molecular manipulations and protein expression. *J Struct Biol* **172**, 34-44 (2010).

64. S. Q. Zheng *et al.*, MotionCor2: anisotropic correction of beam-induced motion for improved cryo-electron microscopy. *Nat Methods* **14**, 331-332 (2017).

65. A. Rohou, N. Grigorieff, CTFFIND4: Fast and accurate defocus estimation from electron micrographs. *J Struct Biol* **192**, 216-221 (2015).

66. J. Zivanov *et al.*, New tools for automated high-resolution cryo-EM structure determination in RELION-3. *Elife* **7**, (2018).

67. J. A. Mindell, N. Grigorieff, Accurate determination of local defocus and specimen tilt in electron microscopy. *J Struct Biol* **142**, 334-347 (2003).

68. G. Tang *et al.*, EMAN2: an extensible image processing suite for electron microscopy. *J Struct Biol* **157**, 38-46 (2007).

69. N. W. Moriarty, R. W. Grosse-Kunstleve, P. D. Adams, electronic Ligand Builder and Optimization Workbench (eLBOW): a tool for ligand coordinate and restraint generation. *Acta Crystallogr D* **65**, 1074-1080 (2009).

70. E. F. Pettersen *et al.*, UCSF chimera - A visualization system for exploratory research and analysis. *J Comput Chem* **25**, 1605-1612 (2004).

71. P. Emsley, K. Cowtan, Coot: model-building tools for molecular graphics. *Acta Crystallogr D* **60**, 2126-2132 (2004).

72. D. Liebschner *et al.*, Macromolecular structure determination using X-rays, neutrons and electrons:

recent developments in Phenix. *Acta Crystallogr D* **75**, 861-877 (2019).

73. P. V. Afonine *et al.*, Real-space refinement in PHENIX for cryo-EM and crystallography. *Acta Crystallogr D* **74**, 531-544 (2018).

74. V. B. Chen *et al.*, MolProbity: all-atom structure validation for macromolecular crystallography. *Acta Crystallographica Section D* **66**, 12-21 (2010).

75. J. Lee *et al.*, CHARMM-GUI Input Generator for NAMD, Gromacs, Amber, Openmm, and CHARMM/OpenMM Simulations using the CHARMM36 Additive Force Field. *Biophys J* **110**, 641a-641a (2016).

76. M. A. Lomize, I. D. Pogozheva, H. Joo, H. I. Mosberg, A. L. Lomize, OPM database and PPM web server: resources for positioning of proteins in membranes. *Nucleic Acids Res* **40**, D370-D376 (2012).

77. M. O. W. Grimm *et al.*, From brain to food: Analysis of phosphatidylcholins, lyso-phosphatidylcholins and phosphatidylcholin plasmalogens derivates in Alzheimer's disease human post mortem brains and mice model via mass spectrometry. *J Chromatogr A* **1218**, 7713-7722 (2011).

78. D. Van der Spoel *et al.*, GROMACS: Fast, flexible, and free. *J Comput Chem* **26**, 1701-1718 (2005).

79. J. Huang *et al.*, CHARMM36: An Improved Force Field for Folded and Intrinsically Disordered Proteins. *Biophys J* **112**, 175a-176a (2017).

80. M. Igaev, C. Kutzner, L. V. Bock, A. C. Vaiana, H. Grubmuller, Automated cryo-EM structure refinement using correlation -driven molecular dynamics. *Eur Biophys J Biophy* **48**, S126-S126 (2019).

81. W. Humphrey, A. Dalke, K. Schulten, VMD: Visual molecular dynamics. *J Mol Graph Model* **14**, 33-38 (1996).

82. R.A. Friesner, *et al.*, Extra Precision Glide: Docking and Scoring Incorporating a Model of Hydrophobic Enclosure for Protein-Ligand Complexes. *J. Med. Chem.* **49**, 6177–6196 (2006).

83. S. Kim S *et al.*, PubChem in 2021: new data content and improved web interfaces. *Nucleic Acids Res.* **49**(D1), D1388–D1395 (2021).

84. Schrödinger Release 2021-1: LigPrep, Schrödinger, LLC, New York, NY (2021).

85. G.M. Sastry, *et al.*, Protein and ligand preparation: Parameters, protocols, and influence on virtual screening enrichments. *J. Comput. Aid. Mol. Des.* **27**(3), 221-234 (2013).

86. A. Christopoulos and T. Kenakin. G Protein-Coupled Receptor Allosterism and Complexing. *Pharmacol Rev.* **54**, 323-374 (2002).

87. M. Landau *et al.* "ConSurf 2005: The Projection of Evolutionary Conservation Scores of Residues on Protein Structures." *Nucleic Acids Res.* **33**, 299–302 (2005).

88. K. Wade *et al.*, Prevalence and expressivity of loss of function mutations in the Melanocortin 4 Receptor (MC4R) in a UK birth cohort. *medRxiv*, 2020.2010.2030.20220467 (2020).

Acknowledgements: We thank Dr. Nadav Elad for the technical support in microscope operation. We thank Prof. Deborah Fass and Prof. Amnon Horovitz for their helpful discussions and insights.

Funding: This work was funded by the Abisch Frenkel and the Minerva Stiftung Foundations for M.S-B. M.S-B holds the Tauro Career Development Chair in Biomedical Research. M.S-B is supported by the Zuckerman STEM Leadership Program, by Ilse Katz Institute for Material Sciences and Magnetic Resonance Research, the Helen & Milton A. Kimmelman Center for Biomolecular Structure & Assembly, the Joseph and Wolf Lebovic Lab, Dov and Ziva Rabinovich Endowed Fund for Structural Biology, the Harmstieg New Scientist Fund, the Pearl Welinsky Merlo Foundation and by Paul and Tina Gardner. H.I. is the recipient of the Glassman fellowship. M.Y.N is supported by ISF grants #1129/19. F.F is the recipient of S.A. Schonbrunn Fellowship Fund. L.F.C was supported by The Medical Research Council (MRC) UK/Academy of Medical Sciences Clinician Scientist Grant (G0802796). D.B-Z is supported by the Zuckerman STEM Leadership Program. P.J.M was supported by the BBSRC (BB/R006946/1) and MRC

(MR/S008608/1). N.R. is funded by an MRC DTP, and V.C. is funded by an MRC-Barts Charity iCase award (MRC0227). M.S-B, M.Y.N. and P.J.M. are members of the EU funded ERNEST COST action CA18133.

Author contributions: H.I prepared the MC4R-G_s complex with the help of O.D and under the supervision of M.S-B; P.V purified ScFv16; O.D prepared grids, obtained cryo-EM data, processed data, and modeled the structure under the supervision of M.S-B; Y.P. and M.S-B cloned MC4R constructs, mutants and G_s chimera, and optimized conditions for protein expression; F.F performed and analyzed molecular dynamics simulations and docking under the supervision of M.Y.N; J.B, A.G. and V.C performed the cAMP accumulation assays and N.R analyzed the surface expression of receptors by means of flow cytometry analysis under the supervision of P.J.M and L.F.C; M.S-B, P.J.M, M.Y.N and D.B-Z conceptualized the study; M.S-B and P.J.M wrote the manuscript with the help of H.I, O.D and F.F. All authors provided input for the final manuscript version.

Competing interests: The authors declare no competing interests.

Data and materials availability: The cryo-EM density map has been deposited in the Electron Microscopy Data Bank (EMDB) under accession code EMD-11927, and model coordinates have been deposited in the Protein Data Bank (PDB) under accession no. 7AUE. All other data are available in the manuscript or supplementary materials. Materials are available from M.S-B and P.J.M. upon request.

Figure Legends

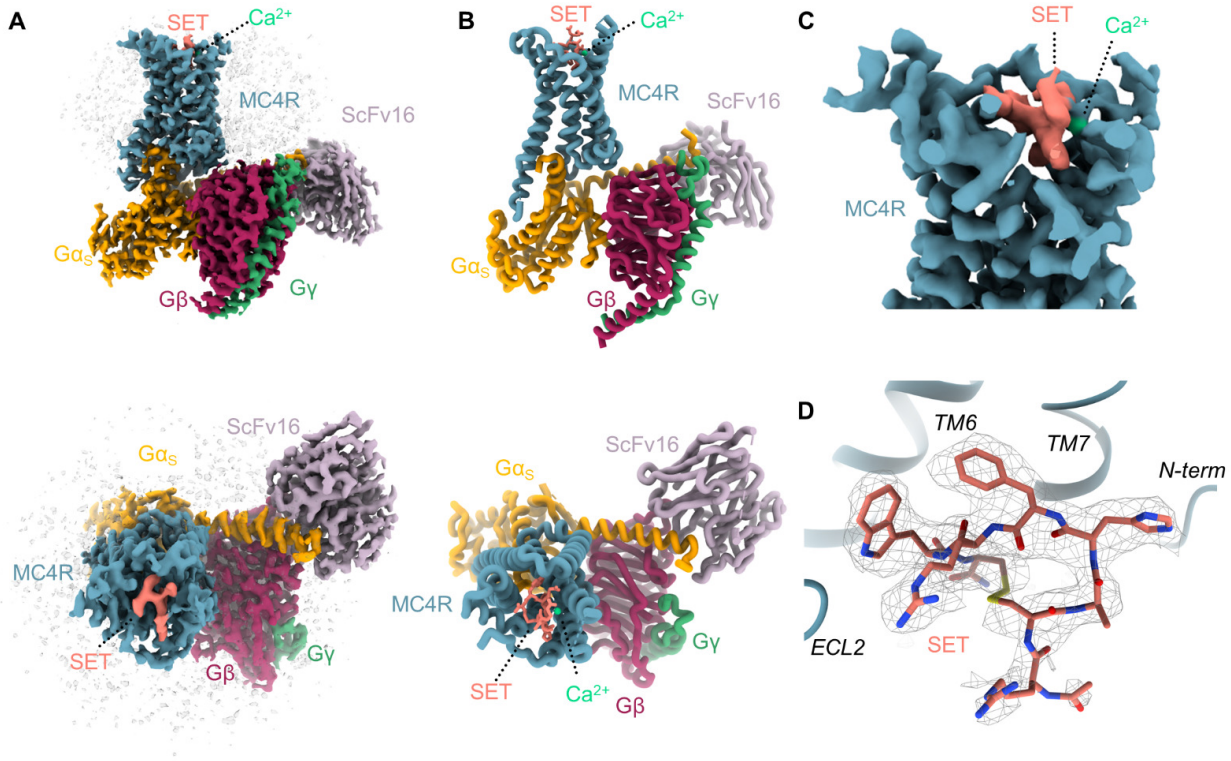

Fig. 1 An overall description of MC4R architecture. (**A**) Cryo-EM map of the MC4R-G_s signaling complex embedded within an LMNG:GDN micelle. MC4R is in blue, Setmelanotide (SET) in pink and $G\alpha_s$, β and γ are in yellow, magenta and green, respectively. ScFv16 is in light purple. Bottom map is rotated 90º along the X axis. Map contour level is 0.027. (**B**) Cartoon model corresponding to map positions presented in **A**. (**C**) A view of MC4R cryo-EM map with setmelanotide in the orthosteric binding pocket. Setmelanotide is in pink, density for Ca^{+2} is presented in light green. Map contour level is 0.027. (**D**) Setmelanotide in density. Map contour level is 0.02.

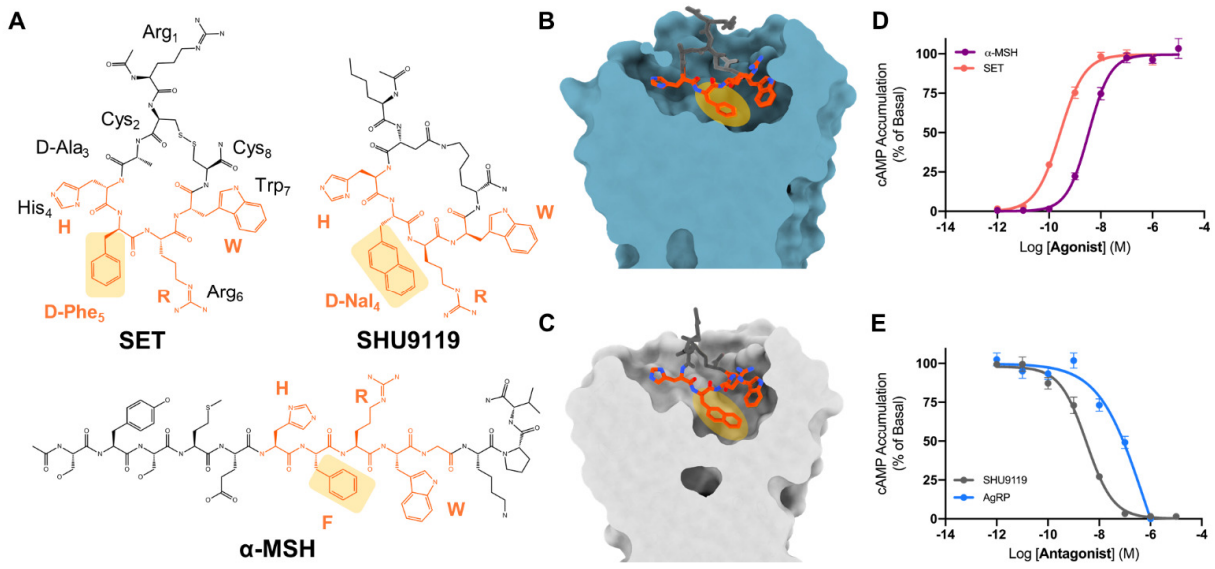

Fig. 2 Agonists and antagonists for MC4R. (**A**) Chemical structures of MC4R agonists α-MSH and setmelanotide (SET) and the antagonist SHU9119. The conserved HFRW motif is in orange. Phenylalanine substitutions in SET (D-Phe$_5$) and in SHU9119 (D-Nal$_4$) are highlighted in yellow. A view of setmelanotide (**B**) and SHU9119 (PDB 6W25) (**C**) at the MC4R orthosteric binding pocket. HFRW motif is in orange with D-Phe$_5$ (SET) and D-Nal$_4$ (SHU9119) highlighted in yellow. Active receptor is in blue (**B**) and inactive in grey (**C**). Comparing the active and inactive receptor states, the D-Nal$_4$ moiety of the antagonist SHU9119 penetrates more deeply into the pocket. (**D**) Dose response curves for the agonists α-MSH (purple) and setmelanotide (pink) measured as cAMP production normalized by % basal activity of the wild-type receptor. Data represented as mean ± SEM from 3 independent experiments done in triplicate, indicating EC$_{50}$ values of 3.79±0.87 nM and 0.29±0.04 nM for α-MSH and setmelanotide, respectively. (**E**) Competition assays of inverse agonists AgRP (blue) and SHU9119 (grey) with α-MSH, calculated as the decrease in cAMP production in the presence of increasing dose of the antagonists. Experiments were conducted in the presence of 1 μM α-MSH. Data represented as mean ± SEM from 3 independent experiments done in triplicate. pIC$_{50}$ values are 6.67±0.18 and 8.51±0.05 nM for AgRP and SHU9119, respectively.

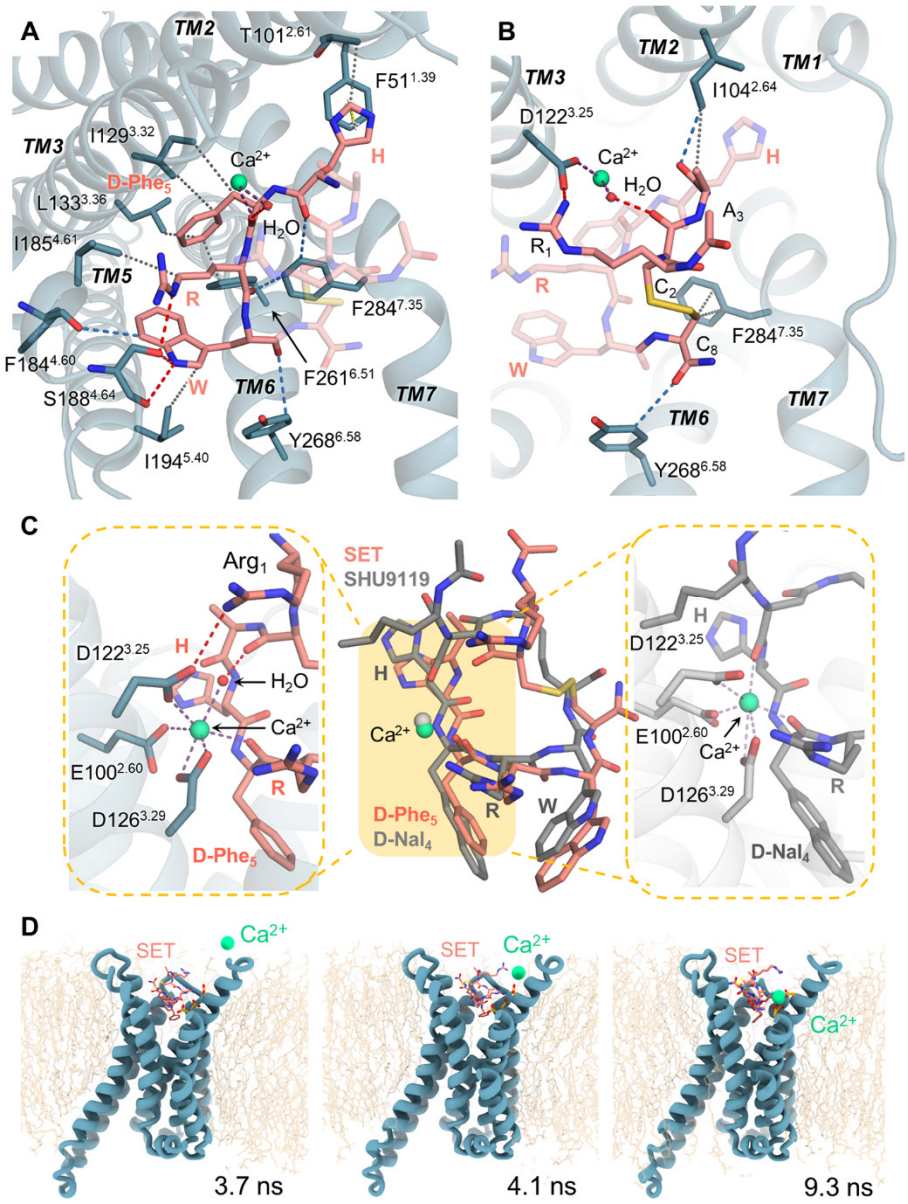

Fig. 3 Ligand accommodation within the MC4R binding pocket. (**A-B**) Setmelanotide interactions in the MC4R binding pocket. The receptor is presented in light blue, setmelanotide (SET) in pink, and Ca^{2+} in green. Dashed lines are colored according to the type of interactions, with hydrogen bonds in red, hydrophobic interactions in grey, CH—O in blue, and Ca^{2+} coordination in purple. π-π stacking is indicated by an asterisk. Interactions with HFRW motif are in **A** and with non-conserved residues in **B**. (**C**) A comparison of the Ca^{2+} coordination in the presence of setmelanotide (agonist, pink, left) and SHU9119 (antagonist, grey, right PDB 6W25). Superposition is of the agonist and antagonist is in the middle. The

receptor is presented as a cartoon with active conformation in light blue and inactive in grey. Ca^{2+} ion is in green for the active and grey for the inactive structure. (**D**) Snapshots of the molecular dynamics equilibration steps after 3.7, 4.1 and 9.3 ns (molecular dynamics run with setmelanotide, replica 1) showing the Ca^{2+} ion (green sphere) entering the ion binding pocket (yellow licorice side chains, showing residues $D122^{3.25}$, $D126^{3.29}$ and $E100^{2.60}$) of the MC4R receptor (light blue cartoon). Setmelanotide shown in pink, the membrane lipids in cream. In the starting configuration of all the simulations, Ca^{2+} was positioned in the intra and extra cellular water layers, leaving the Ca^{2+} binding site free. Out of a total cumulative simulation time of 2 μs, Ca^{2+} was found in the MC4R-bound position for ~1.8 μs and, once binding was established, the ion remained inside the binding pocket throughout the simulations performed (**Fig. S5C-D**).

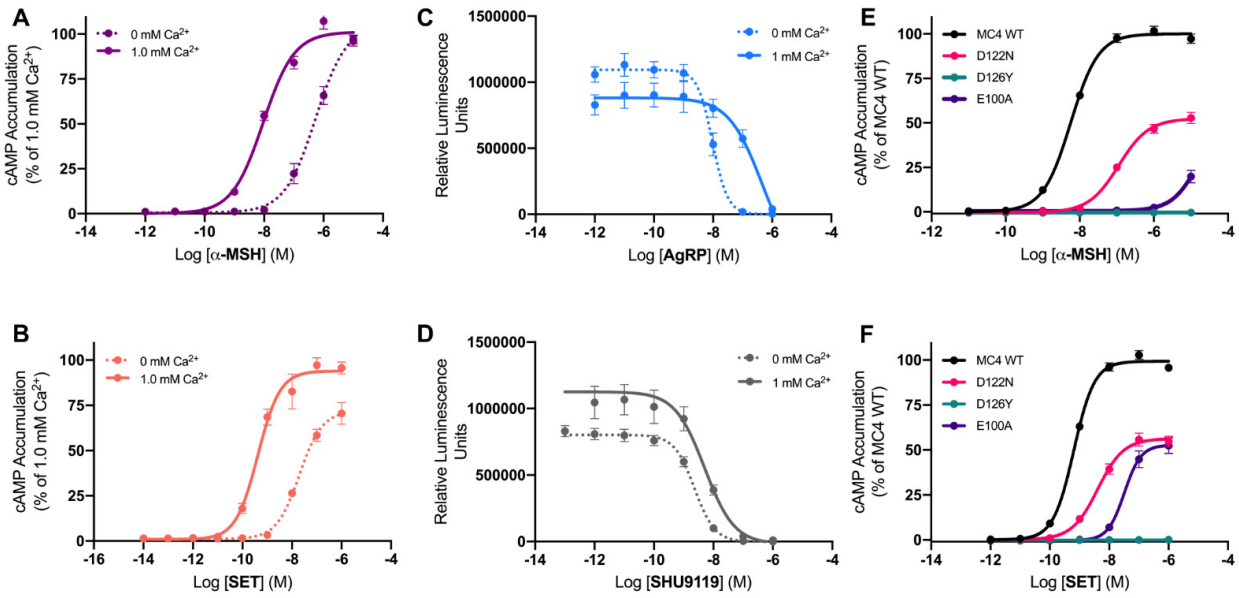

Fig. 4 Ca^{2+} acts as a cofactor for MC4R activation. Dose response curves for the agonists α-MSH (**A**) and setmelanotide (**B**) in the absence and presence of 1 mM Ca^{2+}. The absence of Ca^{2+} is indicated with a dashed line. Data represented as mean ± SEM from 3 independent experiments done in triplicate. (**C-D**) Competition assays of antagonists AgRP (**C**) and SHU9119 (**D**) with α-MSH in the absence and presence of 1 mM Ca^{2+}. Assays are calculated as the decrease in cAMP production in the presence of increasing dose of the antagonists. Experiments were conducted in the presence of 1 μM α-MSH. Data represented as mean ± SEM from 3 independent experiments done in triplicate. (**E-F**) Mutations in residues involving Ca^{2+} coordination significantly reduce receptor's activation through α-MSH (**E**) and setmelanotide (**F**). Dose response curves for the agonists indicate elevation in cAMP production and are represented as mean ± SEM from 3 independent experiments done in triplicate. Cell cytometry analysis indicating surface expression of wild-type and mutants is in **Fig. S8D**. Mutant dependence on Ca^{2+} is in **Fig. S8 E-F**.

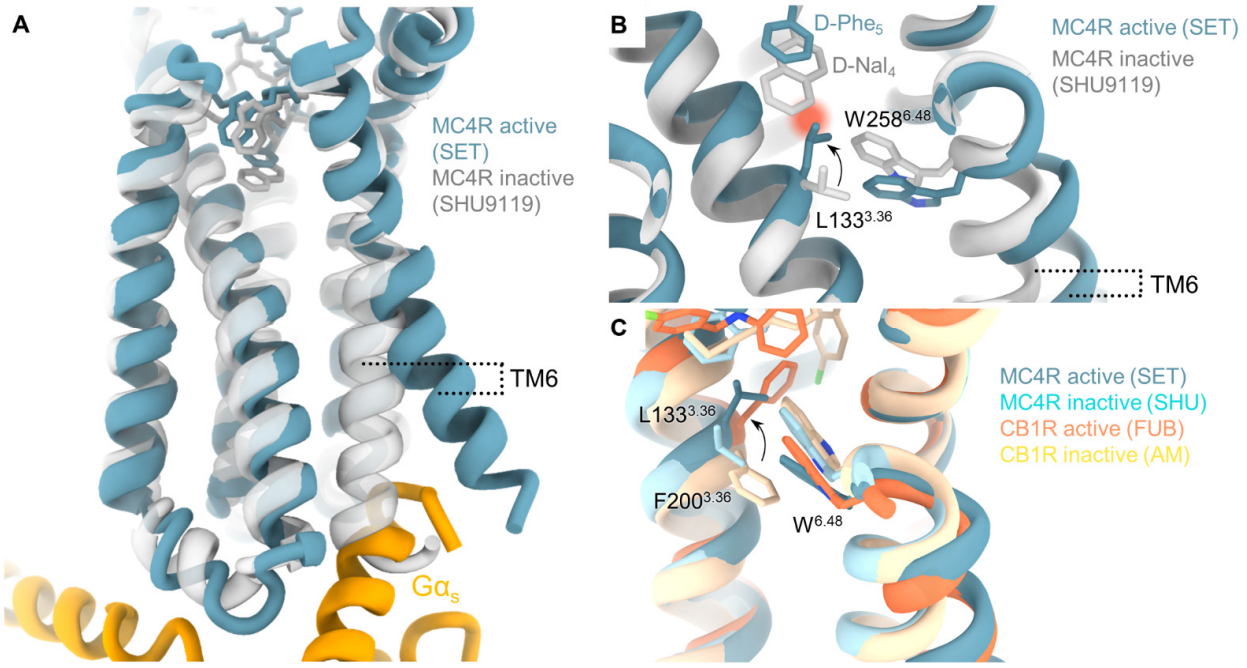

Fig. 5 MC4R activation switch. (**A**) Superposition of the MC4R active complex (blue) with an antagonist bound receptor (SHU9119, PDB 6W25, grey). Setmelanotide (SET, blue) and SHU9119 (grey) bound at the MC4R canonical pocket differentially interact with L133$^{3.36}$ that composes the switch that controls receptor conformation. The outward movement of TM6 is indicated by black dashed lines, Gα_s is in yellow. (**B**) The bulky D-Nal$_4$ moiety in SHU9119 stabilizes the inactive switch conformation (grey), by which L133$^{3.36}$ is stacked upon W258$^{6.48}$. The D-Phe$_5$ moiety in setmelanotide contributes to an alternative rotamer, releasing W258$^{6.48}$ which enables the outward movement of TM6 to allow the accommodation of Gα_s and receptor activation (blue). The arrow indicates switch alternation from the inactive to the active state. (**C**) Superposition of MC4R activation switch (active - blue, inactive - light cyan) with a classical 'toggle twin switch' of CB1R (PDB 6N4B and 5TGZ, for active - orange, and inactive - light yellow conformations, respectively). The comparison between the two switches indicates a similar conformation of the two switches despite the difference in the identity of the switch residues. In MC4R the switch is composed of L133$^{3.36}$ and W258$^{6.48}$, whereas the classical switch in CB1R is composed of F200$^{3.36}$ and W356$^{6.48}$.

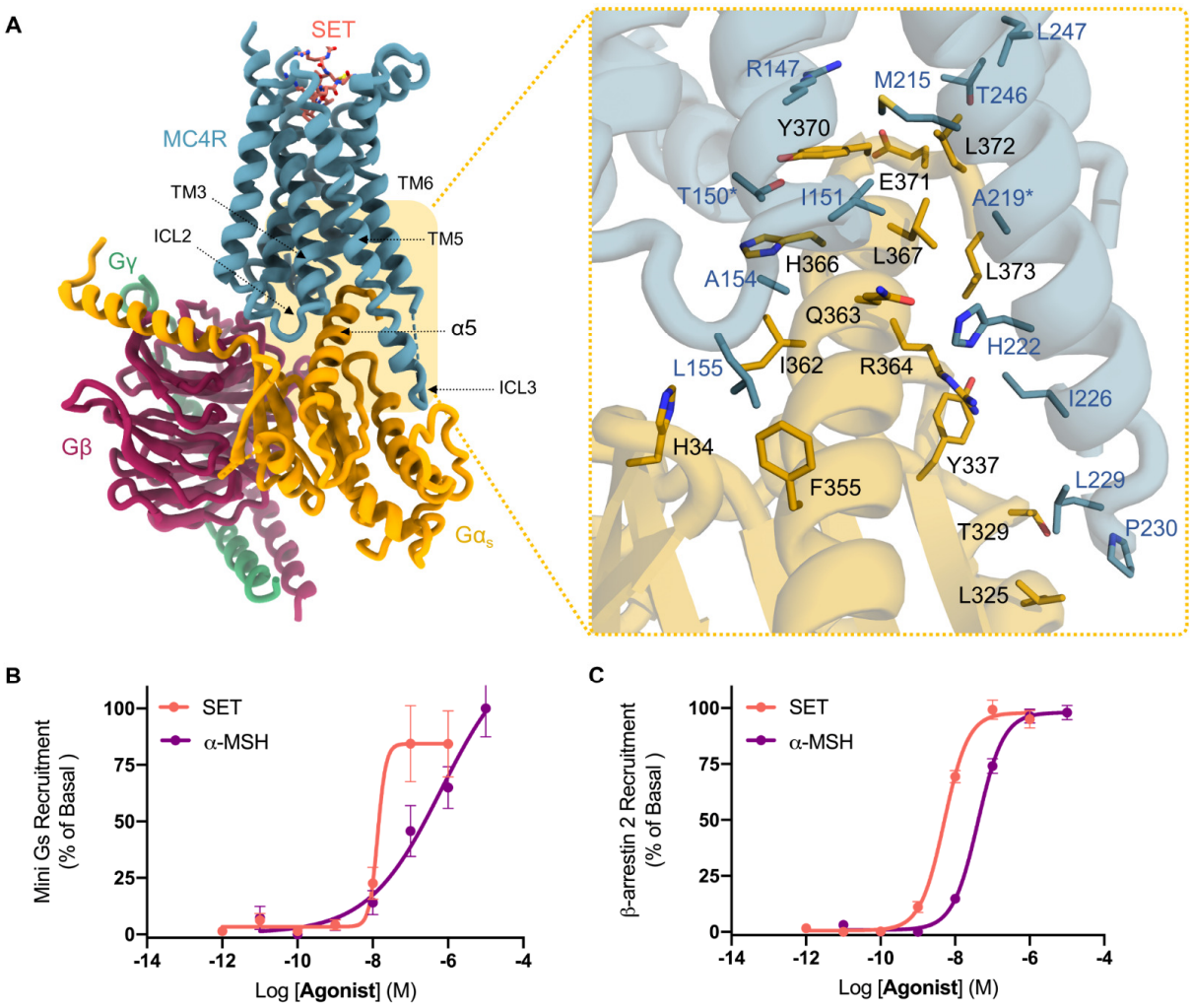

Fig. 6 MC4R G-protein coupling and biased signaling. (**A**) Analysis of residues in MC4R involved in G_s recruitment. Residues in MC4R which are discussed in the main text are highlighted with an asterisk. A full description of interaction is provided in **Fig. S10**. (**B**) Mini-G_s recruitment upon setmelanotide and α-MSH binding. Recruitment was monitored by nano-luciferase complementation using an MC4R-LgBit and a mini-G_s smBit. (**C**) β-arrestin 2 recruitment to MC4R. β-arrestin 2 was monitored by nano-luciferase complementation using an MC4R-LgBit and β-arrestin 2-smBit in HEK293 cells and plotted as a change in luciferase over time. For both **B** and **C** Y-axis is presented as a percent of basal as plotted in dose response curves for the agonists indicated and are represented as mean ± SEM from 3 independent experiments done in triplicate. Analysis in the absence and presence of Ca^{2+} is provided in **Fig. S6K-L**.

Supplementary Materials for

Structure Reveals the Activation Mechanism of the MC4 Receptor to Initiate Satiation Signaling

Hadar Israeli*, Oksana Degtjarik*, Fabrizio Fierro, Vidicha Chunilal, Amandeep Kaur Gill, Nicolas J. Roth, Joaquin Botta, Vadivel Prabahar, Yoav Peleg, Li F. Chan, Danny Ben-Zvi†, Peter J. McCormick†, Masha Y. Niv†, Moran Shalev-Benami†

*These authors contributed equally to this work

†Corresponding authors. Email: moransb@weizmann.ac.il (M.S.B.); p.mccormick@qmul.ac.uk (P.J.M); masha.niv@mail.huji.ac.il (M.Y.N.); dannyb@ekmd.huji.ac.il (D.B-Z.)

This PDF file includes:

Materials and Methods

Construct design and cloning

For the structural studies, human *MC4R* cDNA (hMC4R, ORFeome 90/90 collection) was cloned into pFASTBAC1 (bac-to-bac, Thermofischer Scientific) containing a 3C protease sequence followed by a C-terminus hexa-histidine tag. Cloning was performed using EcoRI-XbaI restriction endonucleases following amplification of the hMC4R cDNA. The following primers were used: 5'-GGATCCCGGTCCGAAGCGCGCGGAATTCATGGTGAACTCCACCCACCGTGGGATGC-3' (forward); 5'TACCTTCTAGATTAGTGATGGTGATGATGGTGTCCGGAGCCGCTTGGACCCTGGAACAGTACCTCAAGATATCTG CTAGACAAGTCACAAAGGCC-3' (reverse). $G\alpha_s$ (human) was modified with the N-terminal helix of $G\alpha_{i1}$ ($G\alpha_{s\text{-}Ni}$) as in Madea et al. (*24*) and was cloned in pFASTBAC-dual under polyhedrin promoter that also contained Ric8a under a secondary MCS. Cloning was performed by the restriction-free (RF) method as in Unger et al. (*63*) using 5'-GATCGACCGCAACCTCCGTGAGGACGGCGAGAAGGCGGCGGCCACGCACCGCCTGCTGCTGCTGGGTGCTG-3' (forward); 5'-GATCGACCGCAACCTCCGTGAGGACGGCGAGAAGGCGGCGGCCACGCACCGCCTGCTGCTGCTG GGTGCTG-3' (reverse) primers. A construct with WT $G\alpha_s$ was a generous gift of Prof. Gregory Tall. Rat $G\beta_1$ with an N- terminal hexa-histidine tag and human $G\gamma_2$ in pFASTBAC-dual and ScFV16 in pVL1393 were cloned as in Madea et al. (*24*). Virus production has been conducted using the bac-to-bac system (Thermofischer Scientific) for the pFASTBAC constructs or the BestBac 2.0 linearized DNA system (Expression systems LLC) for pVL1393. Viruses were prepared according to manufacturer's instructions in *Spodoptera frugiperda* (SF9) cells grown at ESF921 media (Expression systems LLC).

For the signaling assays the pcDNA3.1 plasmid encoding the *N*-terminal 3xHA-tagged human MC4R was obtained from the cDNA Resource Centre (#MCR040TN00). Mutagenesis was generated by TPCR using the reverse primers: 5'-TAATAGGGTGATGACA ATGGTTGCTGATCCATTTGAAACGCTCACC-3' (E100A); 5'-GATCACCGAGTCAATGACATTATTAATATTCACTG TGAAACTCTG-3' (D122N); 5'-CAAGGAGCTACAGATCACCGAGTAAATGACATTATCAAT ATTCAC-3' (D126Y) and 5'-CAGGCTGCAAATGGATGCAAGCATGGAGCTACAGATCACCGAGTC-3' (L133M). 5'-ATTGACGCAAATG GGCGGTAGGC-3' was used as a forward primer for all reactions.

MC4R fusion constructs were generated using the Gibson assembly method. Linearized PCR products were first generated through the PCR. Detailed information regarding the primers, backbone vectors and inserts are in **Table S5**.

The Sm114 labelled mini-G_s was a kind gift from Dr. Nicholas Holliday, University of Nottingham. The sequences were synthesized in human codon optimized versions by GeneArt and are cloned into pcDNA3.1zeo. The Sm114, NanoBiT tag is between HindIII and BamH1, with the mini G sequence (no start codon) between BamH1 and XbaI. Cloning details regarding the SmBit-β-arrestin 2 are provided in **Table S5**.

Protein expression and purification

hMC4R, $G\alpha_{s\text{-}Ni}$, $rG\beta_1$ and $G\gamma_2$ were co-expressed in *Sf9* cells at a ratio of 1:2:1. The cells were cultured in ESF921 (Expression systems LLC) at 27°C and harvested by centrifugation after 48h. Cell pellets were lysed in a buffer consisting of 20 mM HEPES pH 7.4, 100 mM NaCl, 10 mM $MgCl_2$, 5 mM $CaCl_2$, 100 µM TCEP and protease inhibitor cocktail (PIC, cOmplete™ Protease Inhibitor Cocktail, EDTA Free, Roche). Complex formation was instigated at room temperature for 1h by the addition of 25 mU/mL apyrase (Sigma), 20 µg/mL ScFV16 and 10 µM agonist (Setmelanotide, MedChemExpress). The membranes were then solubilized using 0.5% (w/v) lauryl maltose neopentylglycol (LMNG, Anatrace) and 0.1% (w/v) cholesterol hemisucinate (CHS, Anatrace) in 20 mM HEPES pH 7.4, 100 mM NaCl, 10 mM $MgCl_2$, 5 mM $CaCl_2$, 100 µM TCEP, 10uM agonist and PIC, and was incubated for 1.5h at 4°C. Insoluble material was removed by centrifugation at 37,000 ×g for 30 min and clarified supernatant was incubated with Cobalt resin (TALON® Metal Affinity Resin, TaKaRa) and stirred for 1h at 4°C. Resin was loaded onto a gravity flow column and washed with 20 column volumes of wash buffer containing 20 mM HEPES pH 7.4, 100 mM NaCl, 2 mM $MgCl_2$, 100 µM TCEP, 2 mM $CaCl_2$, 15 mM Imidazole, 0.075% (w/v) LMNG, 0.025% (w/v) glyco-diosgenin (GDN, Anatrace), 0.004% (w/v) CHS and 1 µM agonist. Bound material was eluted in a buffer containing 20 mM HEPES pH 7.4, 100 mM NaCl, 250 mM Imidazole, 2 mM $MgCl_2$, 2 mM $CaCl_2$, 100 µM TCEP, 1 µM agonist, 0.075% (w/v) LMNG, 0.025% (w/v) GDN, and 0.004% (w/v) CHS. Sample was concentrated using an Amicon Ultra Centrifugal Filter (MWCO 100kDa, Merck-Millipore) and loaded onto Superdex200 10/300 GL column (GE Healthcare) with running buffer containing 20 mM HEPES pH 7.4, 100 mM NaCl, 2 mM $MgCl_2$, 2 mM $CaCl_2$, 100 µM TCEP, 10 µM agonist, 0.00075% (w/v) LMNG, 0.00025% GDN and 0.00015% (w/v) CHS. The fractions for the monomeric complex were collected and concentrated individually for the EM-experiments. For the Western blot analysis of MC4R a polyclonal anti-MC4 receptor Ab (Alomone labs) has been used in a 1:400 dilution, with a secondary anti-rabbit-HRP (Jackson ImmunoResearch laboratories) at 1:10,000. Further experimental details are provided in **Fig. S1**.

ScFv16 production

ScFv16 production has been performed as previously described (*24*). In brief, a C-terminus octa-his tagged scFv16 with a 3C cleavage site was expressed in a secreted form of *Trichoplusia ni Hi5* cells (Tni, Expression systems LLC). Cells were grown for 48h at 27°C and harvested by centrifugation. Supernatant was pH adjusted with Tris buffer to pH 7.5 and supplemented with 1 mM $NiCl_2$, 5 mM $CaCl_2$ and PIC. The solution was stirred for 1h at room temperature (RT). and clarified by centrifugation at 5000 rpm for 15 min. The supernatant was loaded onto nickel resin (TaKaRa) and washed with 20 mM HEPES pH 7.5, 500 mM NaCl and 20 mM imidazole. Elution was performed with 20 mM HEPES pH 7.5, 100 mM NaCl and 250 mM imidazole. His tag has been removed by 3C protease cleavage (PreScission Protease from human rhinovirus - HRV 3C; GeneScript) 16h at 4°C while equilibrating through dialysis with 20 mM HEPES pH 7.5 and 100 mM NaCl. Cleaved ScFV16 was further purified through reverse Ni binding that allowed for the removal of the cleaved tag and his-tagged protease and was loaded onto a Superdex200 10/300

GL column (GE Healthcare) with running buffer containing 20 mM HEPES pH 7.4 and 100 mM NaCl. Purified fractions were pooled, concentrated, flash-frozen in the presence of 15% glycerol and kept in -80°C until further use.

Cryo-EM

3.5 μL of purified MC4R-G_s complex at 14 mg/ml were applied on glow-discharged (90 sec, 15 mA, PELCO easiGlow™, TED PELLA Inc.) holey carbon gold grids (Quantifoil R1.2/1.3, 200 mesh). The grids were blotted using a Vitrobot Mark IV (FEI) with 3 s blotting time, 10 sec wait time and blot force -1 at 22°C in 100% humidity, and plunge-frozen in liquid ethane. A total of 10,870 movies were recorded on a Titan Krios electron microscope (Thermofischer Scientific - FEI) operating at 300 kV at a calibrated magnification of x105K and corresponding to a magnified pixel size of 0.86 Å. BioQuantum energy filter (Gatan) was operated with an energy slit width of 20 eV. Micrographs were recorded using a K3 direct electron camera (Gatan) with an exposure rate of ~30.6 electrons/Å^2/s and defocus values ranging from −0.8 μm to −2.3 μm. The total exposure time was 1.49 s and intermediate frames were recorded in 0.033 s intervals resulting in an accumulated dose of ~45.5 electrons per Å^2 and a total of 45 frames per micrograph. Automatic data acquisition was done using EPU (Thermofischer Scientific - FEI).

Micrographs were subjected to beam-induced motion correction using MotionCor2 (*64*). CTF parameters for each micrograph were determined by CTFFIND4 (*65*). Initial particle selection in RELION 3.0 (*66*) was done manually followed by particle extraction and 2D classification for a template guided particle picking that resulted in an initial set of 5,076,884 particle projections. The particles were subjected to reference-free two-dimensional classifications (200 classes, tau fudge= 2, 25 iterations) and three-dimensional (3D) classifications (8 classes, tau fudge=4, 25 iterations) in RELION 3.1 (*66, 67*). The map of CB1 receptor (EMDB-0339) low pass filtered to 40 Å was used as an initial reference model for maximum-likelihood-based 3D classifications. Conformationally homogeneous groups accounting for 531,298 particles, forming class averages with well-resolved features, were subjected to 3D refinement by which the alpha-helical domain has been masked out to allow for better particle alignment. Particle sorting was further performed through 3D classification using the refined assignments obtained in 3D refine to allow for the selection of a better homogeneous receptor particle population. The final particle sorting was performed with a mask that encompasses only MC4R. Following these steps, 366,496 particles were used for final map reconstruction, where 3D refinement process was followed by by-particle CTF refinement and Bayesian polishing implemented in RELION 3.1. A binning factor of 2 (pixel size 1.72 Å) was applied during 2D and 3D classifications, for all other processing steps an unbinned data was used with a pixel size of 0.86 Å. A flowchart describing data processing steps is in **Fig. S1**. The final map has an indicated global nominal resolution of 2.97 Å. Reported resolution is based on the gold-standard Fourier shell correlation (FSC) using the 0.143 criterion (**Fig. S2**). Local resolution was determined in RELION 3.1 with half map reconstructions as input (**Fig. S2C**). FSC plots presented in **Fig. S2A** were calculated with EMAN2 (*68*).

Model building and refinement

The initial template of MC4R was derived from the crystal structure of an antagonist-bound MC4R (PDB 6W25). The CB1R receptor coordinates (PDB 6N4B) were used as initial models for the G-proteins and scFv16, where the chimeric $G\alpha_s$ model was generated through homology modeling in swiss model using the CB1R model as template (*26*). Agonist coordinates and geometry restraints were generated using Phenix.elbow (*69*). Models were docked into the EM density map using UCSF Chimera (*70*), followed by iterative manual building in Coot (*71*). The final model was subjected to global refinement and minimization in real space using phenix.real_space_refine implemented in Phenix (rotamer restrains; Ramachandran restrains; Ncs constrains) (*72, 73*). Molprobity (*74*) was used to evaluate model geometry. FSC curves were calculated between the resulting model and the half map used for refinement as well as between the resulting model and the other half map for cross-validation (**Fig. S2B**). The final refinement parameters are provided in **Table S1**.

Signaling assays

Human Embryonic Kidney (HEK293) cells (ATCC® CRL-1573™) were grown in Dulbecco's Modified Eagle's medium (DMEM) - high glucose (Sigma-Aldrich) supplemented with 100 U/mL penicillin, 100 mg/mL streptomycin and 10% (v/v) heat-inactivated Fetal Bovine Serum (PAN Biotech, Germany) at 37°C with 5% CO_2. HEK293 were grown in T-75 cm^2 flasks.

HEK293 cells were transiently transfected following the reverse transfection method using Lipofectamine™ 3000 (Thermofischer Scientific). Cells were washed with DPBS depleted of Ca^{2+} and Mg^{2+}, trypsinised and centrifuged (1000 x g, 5 min, RT). The diluted DNA mix was added to the Lipofectamine™ mix dropwise, and incubated for 15 minutes at RT. The cell pellet was resuspended in 8 mL DMEM-High Glucose media, counted and diluted at a density of 75,000 cells/well. 50 uL of the transfection mix was added into a poly-D-lysine (Sigma-Aldrich) coated white clear F-bottom 96-well plate followed by 100 mL of the cell suspension. The plate was incubated at 37°C in a 5% CO_2 incubator for 24h.

24h post transfection, the cell culture media was removed and the cells were washed with cAMP assay buffer (1X HBSS, 24 mM HEPES, 0.1% (w/v) BSA, 3.96 mM $NaHCO_3$, 1 mM $MgSO_4$, 1.3 mM $CaCl_2.2H_2O$). The plate was then equilibrated for 1h at 28°C with 90 mL of cAMP Buffer supplemented with 0.45 mg/mL of Firefly D-Luciferin free acid (NanoLight Technology). Where the use of antagonist was incorporated into the assay, 80 uL of D-Luciferin buffer was used to equilibrate, thereafter 10 mL of the antagonist was pre-incubated for 15 minutes before stimulating the cells with an agonist. Bioluminescence was measured using the CLARIOstar® Plus Plate Reader (BMG LabTech, Germany). Before injecting the treatment ligand, 6 to 10 basal readings were performed until stabilization was reached. An average of these basal reads was used to normalize the response of each well. Bioluminescence was measured for a total of 66 cycles (1 min per cycle), with one second integration time and no lens.

In the case of testing the effects of divalent ions, 24h after transfection, the cell culture media was removed and the cells were washed with cAMP assay buffer (1X HBSS, 24 mM HEPES, 0.1%

(w/v) BSA, 3.96 mM $NaHCO_3$). Thereafter, the cAMP buffer was supplemented with 0.45 mg/mL of Firefly D-Luciferin free acid and the ion being investigated was added (1 mM Ca^{2+}, 0.01 mM Zn^{2+} or 0.2 mM Mg^{2+}). In a 96-well plate assay, half the wells were equilibrated with cAMP buffer without the ions being investigated and the other half in the presence of the ion. The plate was incubated for 1h at 28°C, before initiating the bioluminescence basal readings. However, if the assay incorporated the use of an antagonist, 10 mL was injected and incubated for 15 minutes at 28°C. An average of these basal reads was used to normalize the response of each well. As soon as 10 mL of agonist treatment was injected, bioluminescence was measured for a total of 66 cycles (1 min per cycle) with one second integration time and no lens.

The K_B of Ca^{2+} was calculated by performing cross-titration curves of α-MSH and Ca^{2+} (0 – 1mM) and then using Graph Pad Prism to calculate K_B using a nonlinear regression analysis fit to an allosteric EC_{50} shift model (**Fig. S6M**).

Mini-G_s recruitment assays

HEK 293 cells (75,000 cells/well) were seeded in poly-D-lysine coated white bottom 96-well plate and reverse co-transfected with the plasmid encoding the MC4-LgBiT receptor (50 ng/well) and the SmBiT-Mini G_s fusion at increasing concentrations to decide the optimal conditions required for the assay to function. On the basis of these results, 10 ng/well of the SmBiT-Mini G_s was co-transfected with 50 ng/well of MC4R-LgBiT. 24h post-transfection, the cells were washed once with cAMP assay buffer and the plates were pre-equilibrated for 1h at 37°C with 90 µL of cAMP assay buffer per well. 25 µL/well of a 5X solution of the Nano-Glo® Live cell reagent was added and luminescence readings were taken every minute at 37°C until the signal was stable (3-5 min). Immediately after, 10 µL of agonist/vehicle were added and luminescence was further recorded for 60 min (no lens, 0.5 s integration time and 1 min intervals at 37°C using a CLARIOstar® Plus Multimode Plate Reader (BMG Labtech, Germany). To account for differences in expression/cell density, the average of at least 3 stable pre-readings was used to normalize each well response.

β-arrestin recruitment assays

To establish the optimal receptor: β-arrestin interactor pair, HEK293 cells (75,000 cells/well) were seeded in poly-D-lysine coated white clear bottom 96-well plates and reverse co-transfected with the plasmids encoding the receptor (50 ng/well) and the β-arrestin 2 fusions at increasing concentrations to account for differences in the total amount of DNA/well. On the basis of these results, 10 ng/well of SmBiT-β-arrestin 2 was co-transfected with 50 ng/well of MC4R-LgBiT. 24h post-transfection, the cells were rinsed once with cAMP assay buffer and the plates were pre-equilibrated in the dark for 1h at 37°C with 90 µL of cAMP assay buffer. 25 µL/well of a 5X solution of the Nano-Glo® Live cell reagent was added, and luminescence readings were taken every minute at 37°C until the signal was stable (3-5 min). Immediately after, 10 µL of agonist/vehicle were added and luminescence was further recorded for 60 min (no lens, 0.5 s integration time and 1 min intervals at 37°C using a CLARIOstar® Plus Multimode Plate Reader (BMG Labtech, Germany). To account for differences in expression/cell density, the average of at least 3 stable pre-readings was used to normalize each well response.

Flow cytometry analysis

HEK293 cells were plated into six-well plates, a single well for each mutant. Cells were transfected with MC4R constructs using Lipotransfectamine 3000 (Invitrogen) according to the manufacturer's instructions. After 48h cells were harvested by gentle scraping and washed in PBS. Cells were stained with the Zombie Violet Live / Dead stain (Biolegend) reagent according the manufacturer's instructions. Briefly, the viability stain was diluted 1:1000, cells were spun down and resuspended in 100 µL of the diluted viability stain. Cells were then incubated for 20 minutes at room temperature before quenched and washed in FACS buffer (PBS + 5% Fetal Bovine Serum + 1 mM EDTA + 0.1% Sodium Azide). Samples were then blocked using 5% Bovine Serum Albumin for 1h at 4°C. After blocking cells were further washed in FACS buffer. HA-tag primary mouse antibody staining (Invitrogen) was performed at a 1:5000 dilution in a staining volume of 150 µL for 1h at 4°C. Cells were then washed three times in FACS buffer before secondary staining. Donkey anti-mouse Alexa Fluor 488 (Invitrogen) secondary antibody at a dilution of 1:5000 was incubated with cells for 1h at 4°C in a staining volume of 150 µL per sample. Cells were further washed 3 times in FACS buffer. Samples were then fixed using 4% paraformaldehyde for 10 minutes and washed 3 times in FACS buffer. Samples were finally resuspended in 350 µL PBS and run on a BD LSRFortessa flow cytometer (BD Biosciences). Analysis was performed in FlowJo software (FlowJo LLC).

Molecular dynamics simulations

Classical molecular dynamics simulations were run for MC4R in the presence and absence of setmelanotide and excluding Ca^{2+} from the binding site, the G-protein heterotrimer and scFv16. The input files were prepared with CHARMM_GUI (*75*), using the histidine protonation state predicted by MolProbity (*74*). MC4R was capped with standard N- and C-termini, while setmelanotide with the acetylated N-terminus and the amidated C-terminus. Through the PPM web server (*76*), the protein was oriented within a membrane bilayer with the following lipid composition (adapted from reference (*77*)): cholesterol (144 molecules), DOPE (48), POPC (24), DPPC (15), SSM (15), SOPS (12), LSM (9), NSM (6), DOPC (6), SOPC (6). The systems were solvated using circa 40,000 water molecules and neutralized using a 2 mM $CaCl_2$ for a total of circa 12 positive and 2 negative ions.

The molecular dynamics simulations were performed using GROMACS 2020-2 (*78*). The charmm36m force field (*79*) parameters were employed for protein, peptide, ions and lipids, and the CHARMM TIP3P water model for water. Each complex was energy minimized with three runs of steepest descent, with the maximum minimization step size progressively increased by one order of magnitude (from 0.001 to 0.01 to 0.1 nm). Each minimization was carried out until no further changes in potential energy were detected. Six steps of equilibration, for a total of 10.875 ns were performed. In each step, the harmonic restraints applied to the protein, peptide and lipids were progressively decreased (see **Table S3** for more details), with the only exception was represented by the residues within 5 Å from the G-protein residues. In this case, restraints of 2000 kJ/mol*nm^2

on backbone and side chains were kept from the 2nd equilibration step for the entire equilibration and production runs to avoid conformational rearrangement due to the absence of the G-protein. The temperature in each step was controlled with a Berendsen thermostat and set to 310 K, while from step 3 to 6 the pressure was set to 1 bar and controlled with semi-isotropic Berendsen barostat. Bond lengths to hydrogen atoms were constrained using LINCS. Short range electrostatic and van der Waals interactions were cut off at 1.2 nm, while long range electrostatic interactions were computed using the particle mesh Ewald method. Periodic boundaries were employed.

Four production run replicas of 250 ns were performed for each complex with a time step of 2 fs (see **Table S4**). The molecular dynamics were run in the NVT ensemble using the Nose-Hoover thermostat at 310 K and sampling the trajectories every 50 ps.

A density-guided molecular dynamics simulation was also run using GROMACS 2020-2 (**Table S4**) (*80*). In density-guided molecular dynamics simulations, additional forces were applied to atoms to restrain the three-dimensional structure into the cryo-EM density map. Differently from the classical molecular dynamics previously described, the Ca^{2+} was retained inside the MC4R ion binding site. The complex with setmelanotide, membrane, water and neutralizing ions was generated as for the classical molecular dynamics. Minimization and equilibration procedures were also performed similarly to the classical molecular dynamics, with the exception of the positional restraints applied on all the MC4R atoms, kept to 2000 kJ/mol*nm^2 for the whole equilibration. The cryo-EM map was aligned to the final coordinates of the equilibration step using USCF Chimera (*70*). Using a time-step of 2 fs, a 10 ns density-guided molecular dynamics was run, sampling the trajectory every 10 ps. The cryo-EM map derived forces were applied every 20 steps on the MC4R and setmelanotide atoms, with an adaptive force scaling time constant of 100 ps. Additional parameters were set as described for the classical molecular dynamics.

All the trajectories were analyzed using VMD (*81*) and GROMACS tools.

Docking Experiments

THIQ docking was performed using Glide *(82)* from the Schrödinger Release 2021-1. The structure of the ligand was downloaded from the PubChem database *(83)* and prepared with LigPrep tool *(84)*, resulting in 9 conformations. The MC4R Cryo-EM structure was prepared for docking using the Protein Preparation Wizard *(85)* in Schrödinger. The position of the HFRW tetra-peptide from setmelanotide was used to determine the grids coordinates, setting the size of each grid dimension to 17Å. Two docking grids were built through the Receptor Grid Generation tool, one in the presence and one in the absence of the Ca^{2+} ion. The XP algorithm was employed and the best docking THIQ pose according to the Glide score in each one of the two docking runs, was selected for analysis.

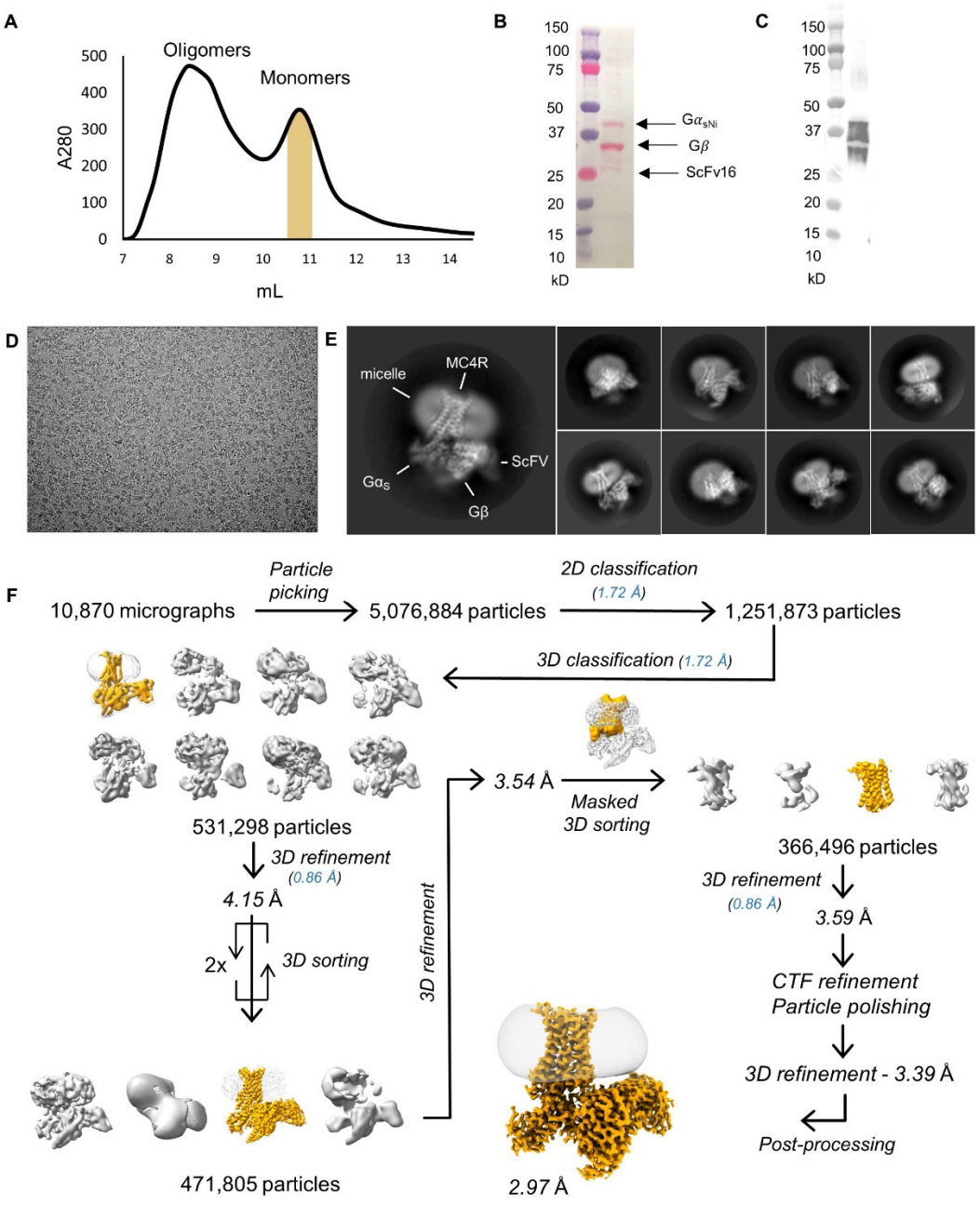

Fig. S1. Cryo-EM flow chart. (A) Size exclusion chromatography (SEC) profile of MC4R complex. Fractions corresponding to the main peak of monomers (yellow) were combined and used for the structural studies. **(B)** Ponceau red stain of the protein complex indicating G-protein and ScFv16. **(C)** Western-blot analysis of the same membrane used in **B** with an anti-MC4R antibody. **(D)** Representative cryo-EM micrograph of the MC4R-G_s complex. **(E)** Representative reference free 2D class averages of the MC4R-G_s complex. The diameter of the circular mask is 20 nm. **(F)** Processing flow chart of MC4R cryo-EM data, including particle selection, 2D and 3D classifications, particle sorting, masking and final map reconstruction. Pixel size is indicated in parenthesis.

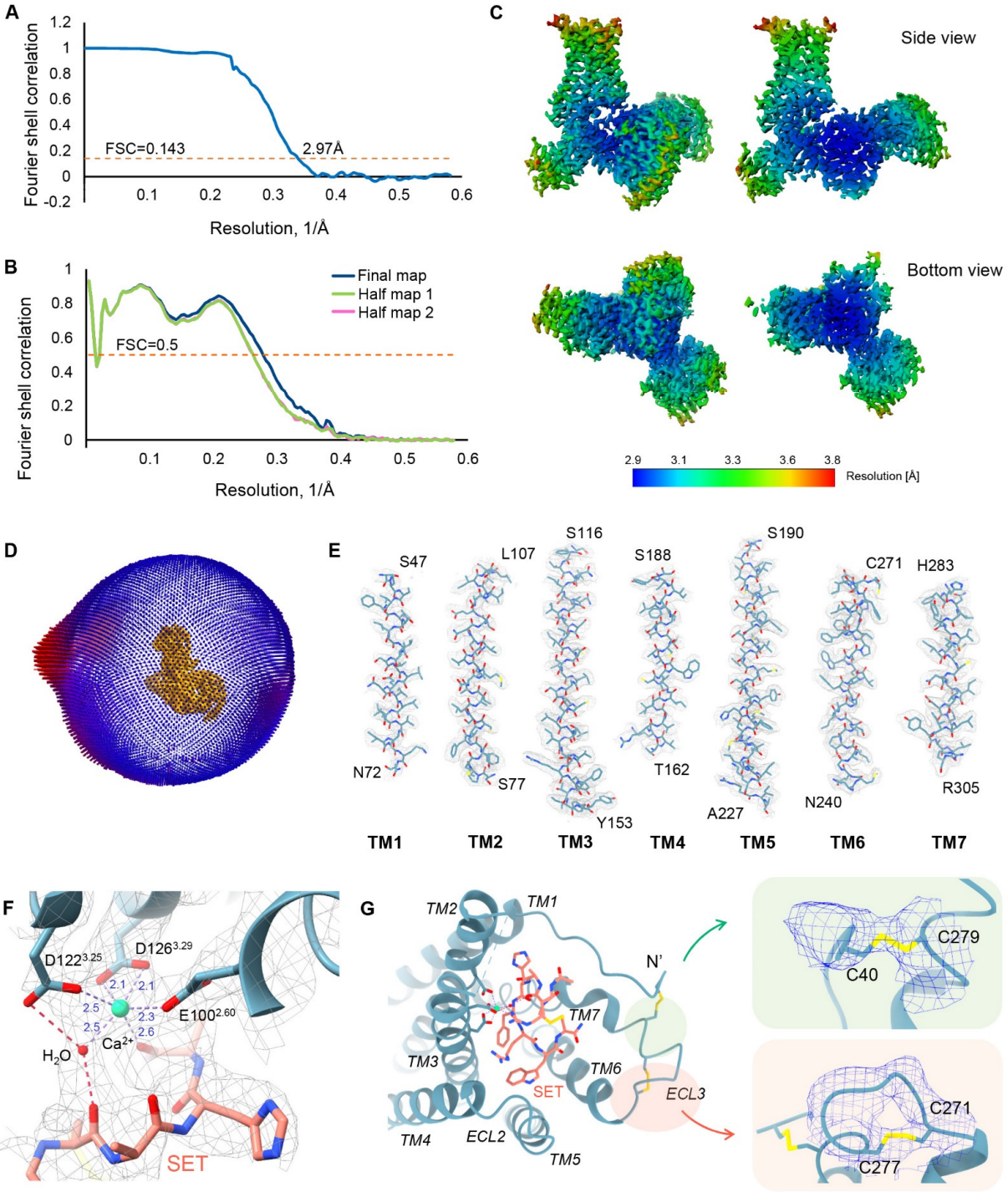

Fig. S2 Map and Model Quality. (A) Gold standard Fourier shell correlation (FSC) curves of half maps that were individually calculated indicating an averaged resolution of 2.97 Å at 0.143 FSC. **(B)** FSC curves of the model *vs.* the final map (blue) and two half maps (green and pink). FSC plots were calculated with EMAN2. **(C)** Final density map colored by local resolution. Color scheme for resolution values is presented in Å. Map contour level is 0.021. **(D)** Euler angle distribution of the cryo-EM reconstruction. **(E)** MC4R helices in density (map contour level

0.021). **(F)** A Ca^{2+} ion (green sphere) is bound within the canonical binding pocket of MC4R maintaining direct interactions with three acidic residues in the receptor $D122^{3.25}$, $D126^{3.29}$ and $E100^{2.60}$, and the peptide backbone of the agonist (SET). The distances are shown in angstroms. Additional contact is through a solvent molecule (red sphere), also observed in our molecular dynamics simulations **(Fig. S5A-B).** MC4R residues are presented in blue, setmelanotide (SET) in pink, EM map is contoured as grey mesh (map contour level 0.021). Residue numbers are indicated in the figure. **(G)** MC4R has two disulfide bridges connecting ECL3 with the N-terminus and TM6 and 7. The two bridges are clearly indicated in our EM map. Density from unsharpened map is presented in blue. Contour levels are 0.00782 and 0.0127 for the upper and lower panels, respectively.

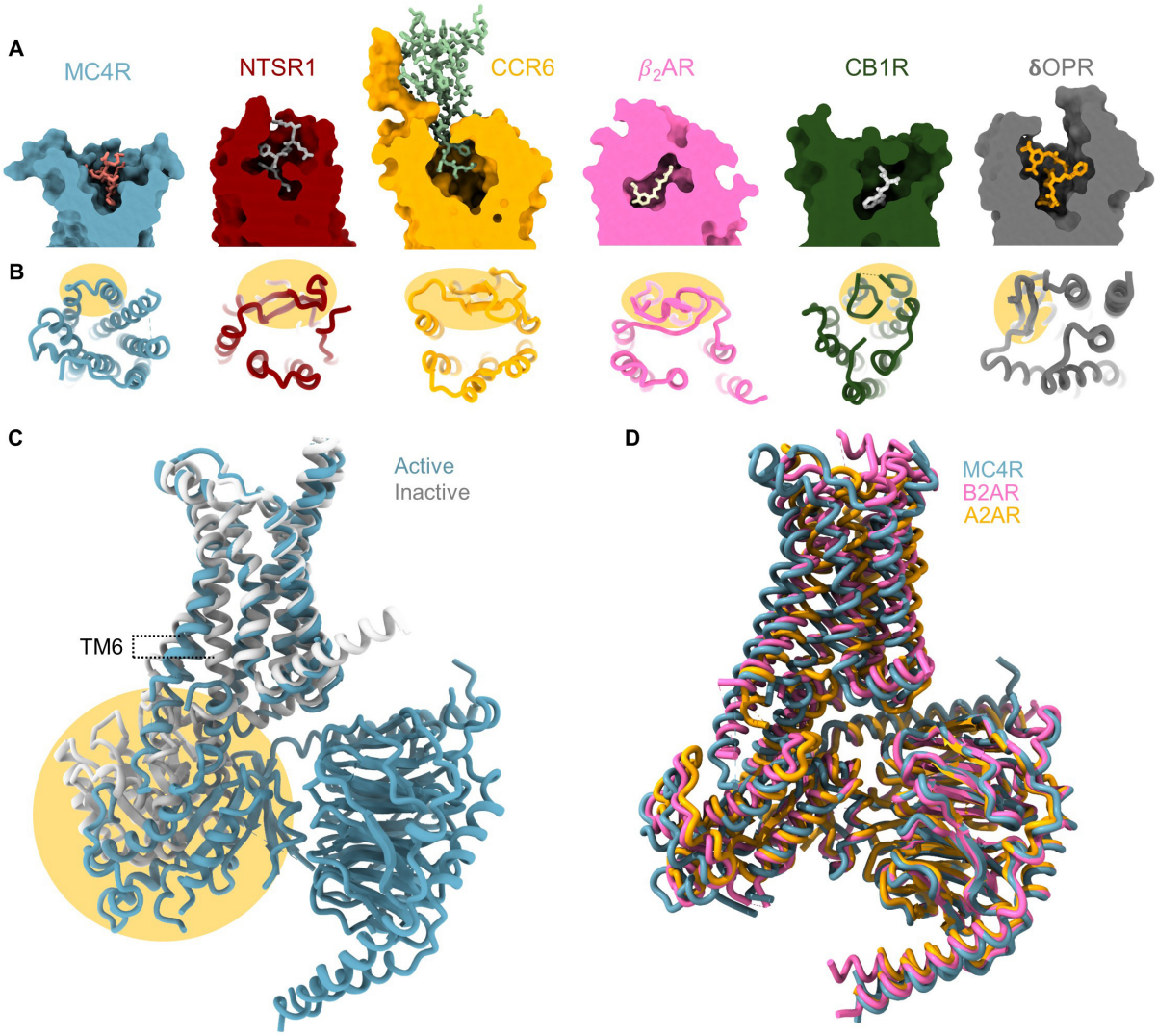

Fig. S3 MCR sequence conservation and comparison with other class-A GPCR members. **(A)** Comparison of binding pocket volumes of selected class-A GPCRs. The MC4R is in blue, the neurotensin receptor 1 (NTSR1, 4GRV) in red, the C-C chemokine receptor type 6 (CCR6, 6WWZ) in yellow, the β2-adrenergic receptor (β2AR, 7BZ2) in pink, the cannabinoid receptor 1 (CB1R, 6N4B) in green and the delta-opioid receptor (μOPR, 6PT2) in grey. All receptors are bound to agonists, thus representing the active conformation. Compared with other class A members MC4R is relatively open, with the ligand exposed to the extracellular milieu. **(B)** Top view of selected class-A GPCRs highlighting the short nature of ECL2 in MC4R and the lack of secondary structure of this loop compared with other receptor subtypes. ECL2 is highlighted yellow. Receptor selection and colors are as in **A**. **(C)** Superposition of active and inactive receptor structures. Inactive receptor (PDB 6W25) is in grey, and the active receptor in blue. Yellow highlight is the overlap between the glycogen synthase moiety used in the crystallographic studies that overlaps with the position of the $G\alpha_s$. **(D)** Superposition of GPCR-G_s complex structures. MC4R in blue, β2 adrenergic receptor (B2AR, 6NI3) in pink and adenosine A2A receptor (A2AR, 6GDG) in yellow. Overlap indicates high conservancy between class members.

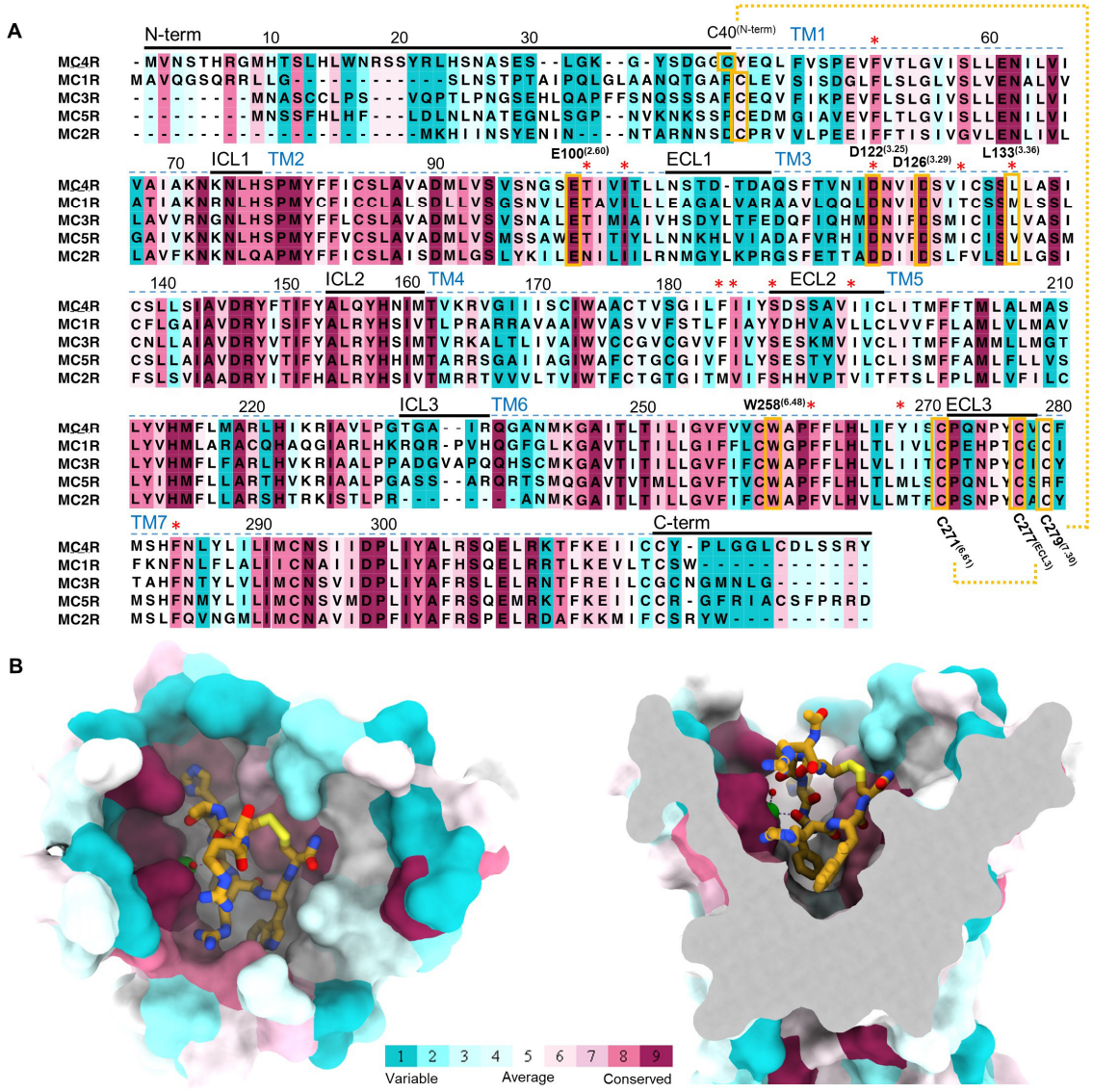

Fig. S4 Sequence and structural conservation of MCRs. (A) Analysis of human MCRs indicating high sequence conservation among family members. Colors are according to the ladder presented in **B** and correspond to the ConSurf analysis (https://consurf.tau.ac.il/) *(87)*. Disulfide bonds common to MCR are highlighted in yellow and connected with a dashed line, residues involved in activation switch and Ca^{2+} coordinating are indicated. Residues involving setmelanotide binding are marked with an asterisk. Numbers are according to MC4R. **(B)** 3D representation of MCR binding pocket with bound agonist. Residues are color coded according to the conservancy level. Setmelanotide is shown in orange. Residues involved in setmelanotide binding are mostly conserved throughout the family and are marked in **A**.

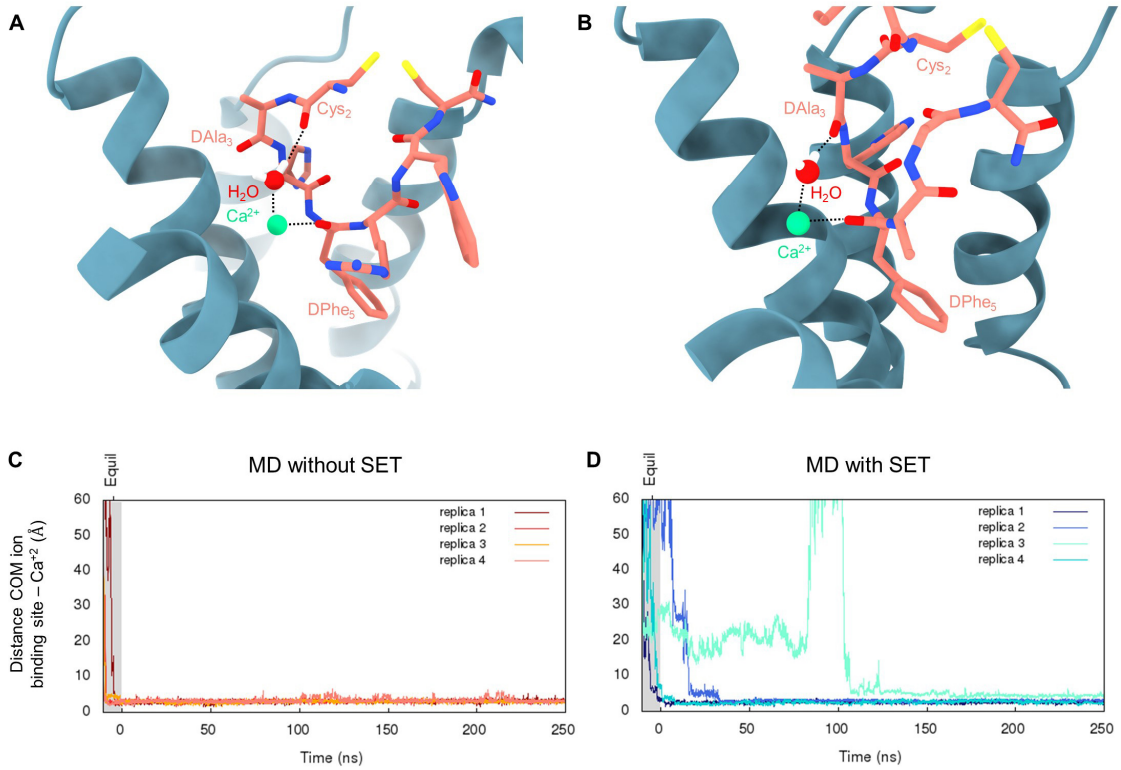

Fig. S5 Molecular dynamics simulations. (A-B) Setmelanotide involvement in Ca^{2+} ion coordination observed during the cryo-EM guided molecular dynamics simulation. Setmelanotide is in pink, Ca^{2+} is presented as a green sphere, MC4R as blue cartoon. Within the cryo-EM guided molecular dynamics simulation, two main conformations were identified: **(A)** Cys_2 was found to interact with the ion through a water mediated hydrogen bond (observed during the first 3 ns). Arg1 is not shown for clarity. **(B)** Cys_2 backbone oxygen rotates in the opposite direction with respect to the ion, the interaction with Ca^{2+} alternates through a hydrogen bond with the backbone oxygen of the D-Ala_3. The D-Phe_5 backbone oxygen interacts with Ca^{2+} in both conformations. **(C-D)** Evolution of the distance between the center of mass of the three ion binding residues ($D122^{3.25}$, $D126^{3.29}$ and $E100^{2.60}$) and the Ca^{2+} during equilibration and production run for the classical molecular dynamics simulations. **(C)** Simulations run without setmelanotide in the binding site show the Ca^{2+} ion entering the binding site during the equilibration step in all 4 replicas. **(D)** Simulations run in the presence of setmelanotide in the binding site indicate that the ion binds the receptor during the equilibration step in 2 out of 4 replicas, while occurring during the production run in replicas 2 and 3. Distances over 60Å are not shown.

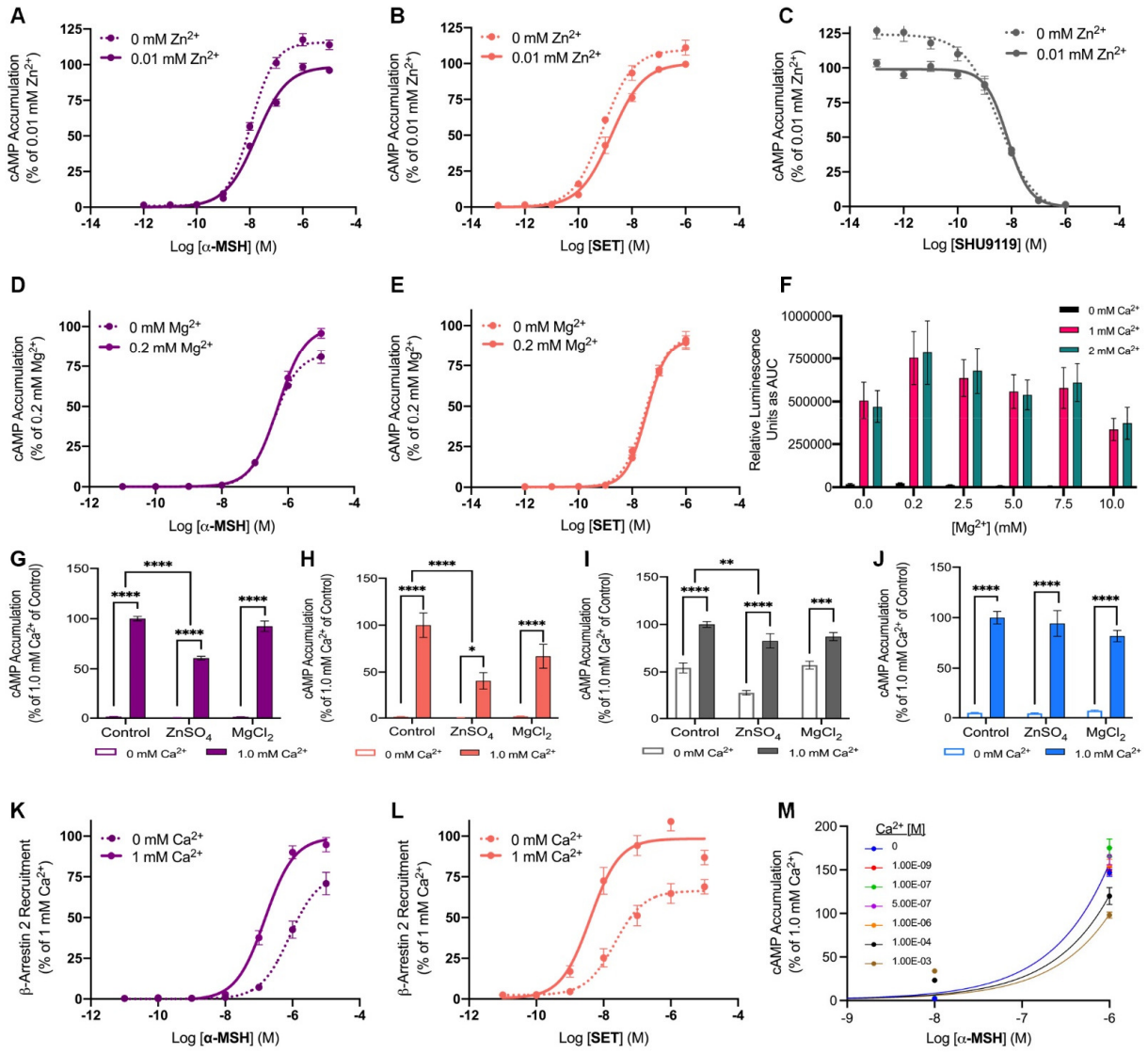

Fig. S6 Signaling assays. HEK293 cells were transfected with WT MC4R and were treated with varying doses of α-MSH **(A)**, setmelanotide **(B)**, or SHU9119 **(C)** in the presence and absence of divalent ions Zn^{2+} **(A-C)** or Mg^{2+} **(D-E)**. In **(F)** a competition assay was performed at fixed concentrations of Ca^{2+} and varying concentrations of Mg^{2+} and cAMP production measured as in the materials and methods by stimulating the cells with a fixed concentration of 0.01 μM α-MSH. In **(G-J)** cAMP production was measured after treating with 0.01 μM α-MSH **(G)**, 0.00025 μM setmelanotide **(H)**, or in the case of **(I-J)** with prior treatment of 0.0032 μM SHU9119 **(I)** or 0.63 μM AgRP **(J)** followed by treatment with 1 μM α-MSH in the presence or absence of Ca^{2+} and +/- 10 μM $ZnSO_4$ or 200 μM $MgCl_2$ as indicated. Statistical significance was evaluated using the two-way (ANOVA) analysis (****$p \leq 0.0001$, ***$p \leq 0.001$, **$p \leq 0.01$ and *$p \leq 0.05$). **(K-L)** β-arrestin 2 recruitment assay upon α-MSH **(K)**, setmelanotide **(L)** binding. Experiments are in 3 independent repeats performed in triplicates. **(M)** Cross-titration curves of Ca^{2+} and α-MSH for MC4R activation. Dose response curves measuring cAMP accumulation after stimulation with the

agonist α-MSH were performed at varying concentrations of Ca^{2+} (see methods). Curves were plotted using the Allosteric EC^{50} shift X is log (concentration) model (based on Christopoulos et al. *(86)*) and fit using the GraphPad Prism 9 software, from which K_B was calculated. Data represented as mean ± SEM from 3 independent experiments done in triplicate.

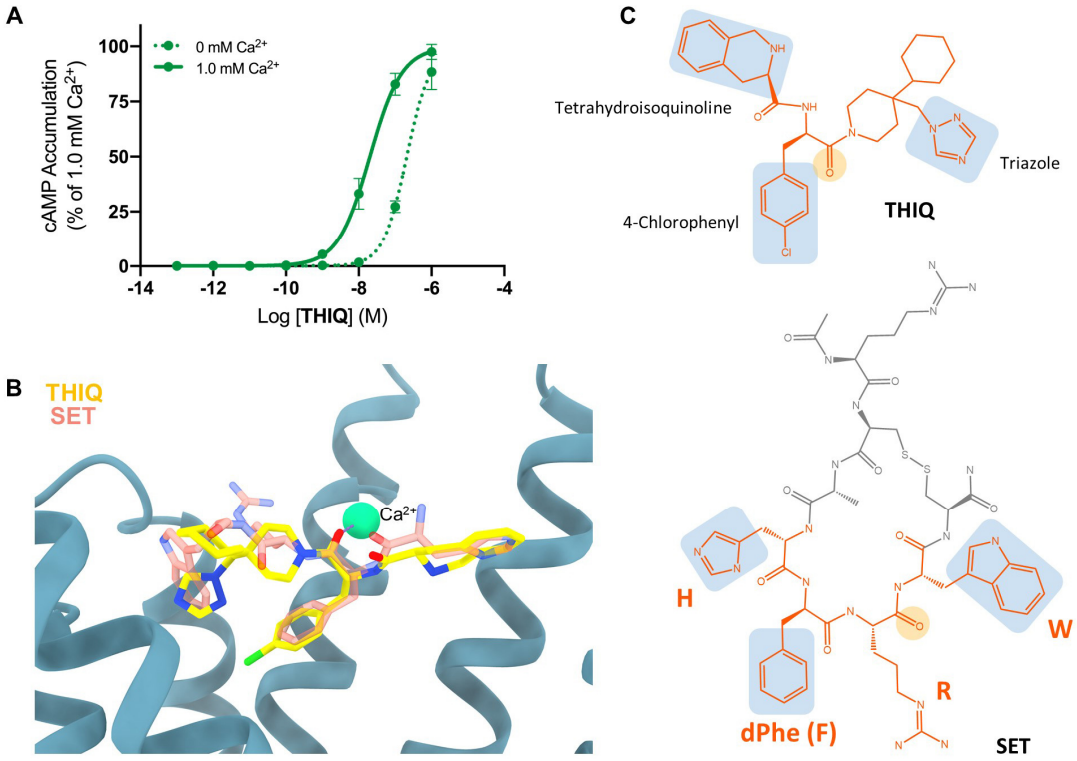

Fig. S7 Activation of MC4R by THIQ depends on Ca^{2+} presence in the binding pocket. (A) cAMP accumulation measured in HEK293 cells in the presence and absence of Ca^{2+} with increasing THIQ concentrations. Experiments have been performed in three repeats in triplicates. **(B)** Superposition of setmelanotide (pink transparent licorice) and docked THIQ (yellow licorice) in the MC4R (blue ribbon) binding pocket, depicting similar traits in Ca^{2+} (green sphere) coordination and ligand binding. For both ligands, the oxygen of a carbonyl group is involved in Ca^{2+} binding. **(C)** Chemical structure of THIQ and setmelanotide (SET). The chemical groups mimicking the conserved HFRW motif side chains within the binding pocket are highlighted in blue, backbone participating in Ca^{2+} coordination is in yellow.

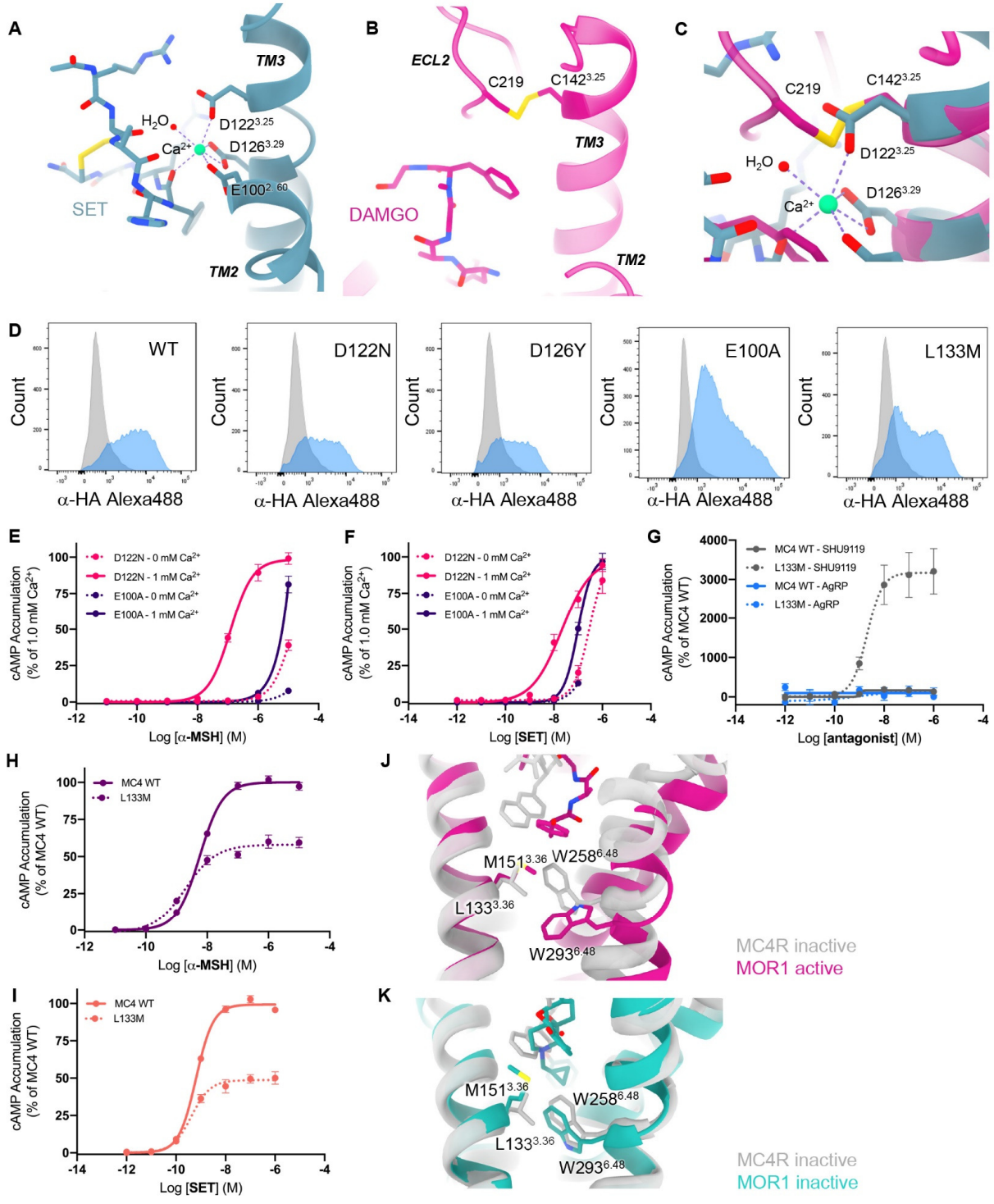

Fig. S8 Ca^{2+} replaces a conserved disulfide and MC4R mutations in key residues. (A-C) $D122^{3.25}$ position overlaps with a cysteine residue forming a disulfide bridge that is conserved in class-A GPCRs. The same bridge is missing in MC4R **(A)**. A typical class-A member, the μ-opioid 1 receptor (MOR1, pink, PDB 6DDE), is presented in **(B)**. Superposition in **(C)** indicates that the coordination of Ca^{2+} serves to replace the bridge in defining the orthosteric binding pocket for

ligand agonists. Residue numbers are indicated in the figures. Agonists (DAMGO for the MOR1 and setmelanotide-SET for MC4R) are presented as sticks. **(E-I)** A series of mutant receptors was designed to study the effect of residues highlighted through structural analysis. In **(D)** surface expression of the WT and mutant receptors was measured by flow cytometry. HEK293 cells were transfected with WT and mutant MC4R constructs as indicated. Cells stained with anti-HA antibodies (blue) are compared to control cells stained only with secondary antibody (grey). The influence of Ca^{2+} presence on MC4R mutants in residues involved in Ca^{2+} coordination is demonstrated in **(E)** for α-MSH and **(F)** for setmelanotide. Experiments performed in the presence or absence of 1 mM Ca^{2+}. Each data point represents the mean ± SEM of at least three replicates (N=3). **(H-K)** $L133^{3.36}$ is a key modulator in class A GPCR activation, as it maintains direct interactions with $W258^{6.48}$ that plays a crucial role in TM6 displacement during receptor transition to the active state. An L133M mutation significantly affects receptor's reactivity to agonists and antagonists. **(G)** Dose response curves for the antagonists SHU9119 and AgRP indicate elevation in cAMP production upon SHU9119 binding to the receptor, but not AgRP. Curves are represented as mean ± SEM from 3 independent experiments done in triplicate. These indicate that SHU9119 (but not AgRP) acts as an agonist rather than as an antagonist in the L133M mutant receptor. Agonist activity of α-MSH **(H)** and setmelanotide **(I)** indicates reduction in E_{max} for both agonists in the mutant receptor. Dose response curves for the agonists indicate elevation in cAMP production and are represented as mean ± SEM from 3 independent experiments done in triplicate. Reduction in receptors activity is mainly due to lower surface availability of the receptor as indicated in **(D)**. **(J)** Superposition of MC4R (grey, PDB 6W25) inactive conformation with MOR1 active (pink, PDB 6DDE) conformation indicates that $M^{3.36}$ in the active state of MOR1 overlaps with that of $L133^{3.36}$ in the inactive MC4R; thus, explaining how an antagonist for MC4R could serve as an agonist for the L133M mutant. **(K)** Superposition of MC4R bound to SHU9119 structure (grey, PDB 6W25) with an inactive structure of the opioid receptor (teal, PDB 4DKL) indicates a clash between the naphthyl group and $M^{3.36}$, thus further supporting the notion that SHU9119 will more likely contribute to an agonistic activity in the mutant.

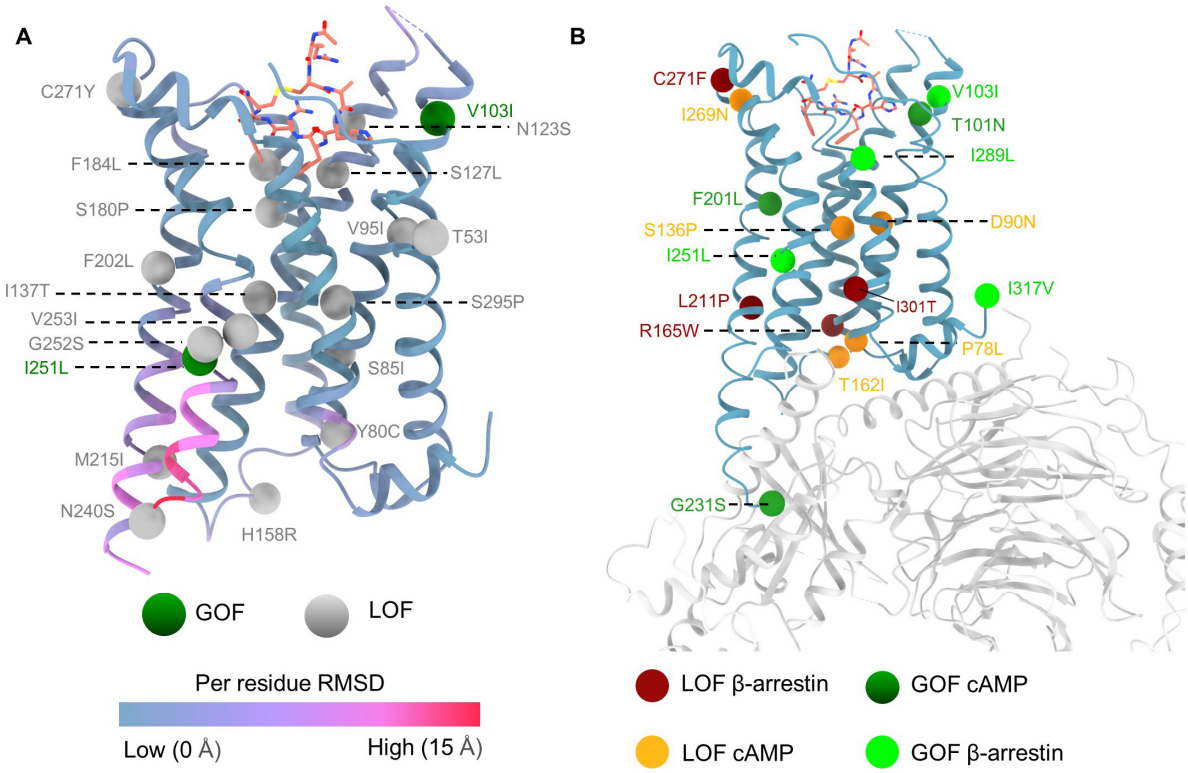

Fig. S9 Mapping of the frequent human MC4R mutations associated with receptor gain-of-function (GoF) and loss-of-function (LoF). (A) Plotting of MC4R mutations on the active cryo-EM structure. Mutations are adopted from Wade et al. (*88*). GoF mutations are represented as green spheres, LoF mutations in grey. MC4R ribbon is colored based on the per-residue RMSD between the active and inactive (PDB 6W25) structures, with blue regions corresponding to highly similar conformations, red to the most diverging regions. Setmelanotide is presented as light pink licorice. Mutations in MC4R that result in impaired receptor signaling spread across multiple receptor regions, and are frequent around the agonist binding pocket (e.g. V103I, N123S, S127L S180P and F184L). Some mutations are also found in regions that are of high residual mobility upon receptor activation. These include M215I, N240S, I251L and G252S. **(B)** Mapping GoF and LoF shown to induce bias to either cAMP or β-arrestin signaling pathways. MC4R is in blue, G-proteins are in light grey. GoF mutations with bias towards cAMP production (G_s) and β-arrestin recruitment are shown in dark and light green, respectively. LoF mutations with impaired cAMP production and low β-arrestin recruitment are shown in orange and dark-red, respectively. Mutations are adopted from the study of Lotta *et al.* (*9*). Examples with mechanistic implications are S136 that stabilizes the toggle switch residue W258 by weak Van der Waals interaction. An S136P LoF would disrupt this interaction and thus affect proper W258 positioning and an impairment of G_s coupling. G231S that is positioned in the interface with G_s resulting in GoF by elevating cAMP levels. Replacement of glycine to serine can increase the affinity to G_s by forming additional contacts. T101N that is positioned in the orthosteric binding pocket and maintains hydrophobic contacts with the HRFW motif. The T101N can increase the affinity to the agonist due to the longer polar side chain thus elevate cAMP accumulation.

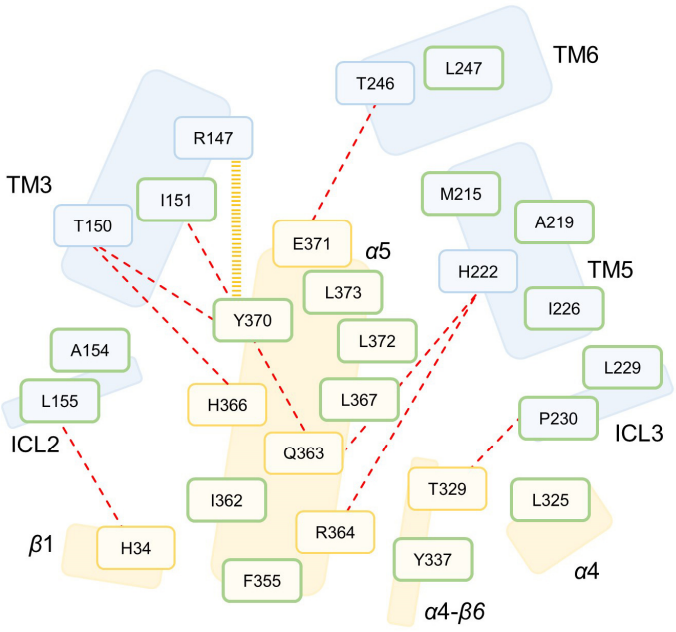

Fig. S10 Schematic representation of the residues involved in MC4R-Gαs coupling. The receptor is shown in blue, $G\alpha_s$ in yellow. Hydrogen bonds are shown as red dashed lines, cation-π interaction in yellow, and hydrophobic interactions are in green. Interactions include hydrogen bonds between $H34^{S1.02}$, $T329^{h4s6.03}$, $Q363^{H5.16}$, $R364^{H5.17}$, $H366^{H5.19}$, $Y370^{H5.23}$ and $E371^{H5.24}$ of $G\alpha_s$ and $T150^{3.53}$, $I151^{3.54}$, $L155^{34.51}$, $H222^{5.68}$, $P230^{ICL3}$ and $T246^{6.36}$ in MC4R. A class-A conserved π-cation stacking between $Y370^{H5.23}$ and $R147^{3.50}$ is also present. Hydrophobic interactions involve residues $F355^{H5.08}$, $I362^{H5.15}$, $L367^{H5.20}$, $Y370^{H5.23}$, $L372^{H5.25}$, $L373^{H5.26}$ of α5, $L325H^{4.16}$ of α4, and $Y337^{h4s6.20}$ of α4-β6 loop of $G\alpha_s$ and residues in TM5 ($M215^{5.61}$, $A219^{5.65}$, $I226^{5.72}$), ICL2 ($A154^{34.50}$ and $L155^{34.51}$), ICL3 ($L229^{ICL3}$, $P230^{ICL3}$), TM3 ($I151^{3.54}$) and TM6 ($L247^{6.37}$) of MC4R.

Table S1 Cryo-EM data collection and model refinement

Data collection and processing	
Microscope	Titan Krios G3i
Detector	Gatan K3
Energy filter slit width [eV]	20
Magnification	105,000
Detector magnification	10,760
Voltage [kV]	300
Electron exposure [e^{-}/Å^2]	45.5
Exposure rate [e^{-}/A^2/sec]	30.6
Defocus range [μm]	-0.8 – (-2.3)
Pixel size [Å]	0.86
Number of frames per movie	45
Automation software	EPU
# Micrographs used	10,870
Initial particle images [no.]	5,076,884
Total # of particles used for 3D analyses	1,251,873
Final particle images [no.]	366,496
Estimated accuracy of translations [Å] / rotations [°]	0.73/1.61
Map resolution (FSC 0.143) [Å]: masked (unmaked)	**2.97** (3.39)
Map resolution (FSC 0.5) [Å]: masked (unmaked)	3.34 (3.94)
Local resolution range in [Å] (Relion)	2.87 – 4.19
Symmetry	P1
Model Refinement	
Refinement package	Phenix
Initial model used (PDB code)	6W25
Model resolution [Å]	2.97
Map sharpening B factor [Å^2]	-107.631
Model composition	
Non-hydrogen atoms	8834
Protein residues	1126 residues
Ligands	1
B factors [Å^2]	
Protein	44.39

Ligand	61.95
R.M.S.D	
Bond lengths [Å]	0.006
Bond angles [°]	1.031
Global and Local CC [CC_{volume}/CC_{mask}]	0.77/0.81
C-beta deviations [%]	0.19
CaBLAM outliers [%]	2.8
EMRinger score [Sharpened/unsharpened map]	3.99/3.79
Validation	
MolProbity score	1.19
Clashscore	1.55
Poor rotamers [%]	0.11
Ramachandran plot	
Favored [%]	95.83
Allowed [%]	7.25
Disallowed [%]	0
PDB/EMDB codes	7AUE/ EMD-11927

Table S2 Unmodeled residues due to low local resolution

MC4R (Chain R)

ECL1	S109, T110, D111, T112, D113, A114
TM3	$Q115^{3.18}$
ICL3	T232, G233, A234, I235, R236
TM6	$Q237^{6.27}$, $G238^{6.28}$, $A239^{6.29}$

Gαs (Chain A)

L56-S184, G205, Q206, R236-Q242

ScFv16 (Chain S)

E222, D223

Table S3 Equilibration parameters for individual runs.

Step	BB restr. (kJ/mol*nm2)	SC restr. (kJ/mol*nm2)	Lipid restr. (kJ/mol*nm2)	Thermostat	Barostat	Timestep (fs)	Duration (ns)
1	4000	2000	1000	Berendsen	/	1	0.125
2	2000	1000	400	Berendsen	/	1	0.125
3	1000	500	400	Berendsen	Berendsen	1	0.125
4	500	200	200	Berendsen	Berendsen	2	0.500
5	200	50	40	Berendsen	Berendsen	2	5
6	50	0	0	Berendsen	Berendsen	2	5

BB=backbone, SC=sidechains, restr.=restraints

Table S4 Summary of the differences among the molecular dynamics simulations performed in this study.

Trajectory name	**Setmelanotide presence**	**Classical MD vs Cryo-EM restraints MD**	**Total length (ns)**	**Ca^{2+} location at time t=0**
MD with SET – replica 1/2/3/4	Yes	Classical	250	Solvent
MD without SET – replica 1/2/3/4	No	Classical	250	Solvent
Cryo-EM restraints guided MD	Yes	Cryo-EM restraints	10	MC4R ion binding site

Table S5 Constructs used in the study and cloning.

Name of Plasmid	Backbone	Backbone Primers (5'→ 3')		Insert	Insert Primers (5'→ 3')	
3x HA-MC4R-SmBiT	CMV-β-arrestin1-SmBiT	FW	GTGACTTGTCTAGCAGATATGGCTCGAGCGGTGGTGGCGG	pcDNA3.1-3xHA-MC4R	FW	AACTTAAGCTTGGTACCACCATGTACCCATACGATGTTCC
		RV	GGAACATCGTATGGGTACATGGTGGTACCAAGCTTAAGTTTAAACGCTAGCCAGC		RV	CCGCCACCACCGCTCGAGCCATATCTGCTAGACAAGTCACA

ATGTACCCATACGATGTTCCAGATTACGCTTACCCATACGATGTTCCAGATTACGCTTACCCATACGATGTTCCAGATTACGCTGATGTGAACTCCACCCACCGTGGGATGCACACTTCTCTGCACCTCTGGAACCGCAGCAGTTACAGACTGC
ACAGCAATGCCAGTGAGTCCCTTGGAAAAGGCTACTCTGATGGAGGGTGCTACGAGCAACTTTTTGTCTCTCCTGAGGTGTTTGTGACTCTGGGTGTCATCAGCTTGTTGGAGAATATCTTAGTGATTGTGGCAATAGCCAAGAACAAGAATC
TGCATTCACCCATGTACTTTTTCATCTGCAGCTTGGCTGTGGCTGATATGCTGGTGAGCGTTTCAAATGGATCAGAAACCATTGTCATCACCCTATTAAACAGTACAGATACGGATGCACAGAGTTTCACAGTGAATATTGATAATGTCATTGA
CTCGGTGATCTGTAGCTCCTTGCTTGCATCCATTTGCAGCCTGCTTTCAATTGCAGTGGACAGGTACTTTACTATCTTCTATGCTCTCCAGTACCATAACATTATGACAGTTAAGCGGGTTGGGATCATCATAAGTTGTATCTGGGCAGCTTGCAC
GGTTTCAGGCATTTTGTTCATCATTTACTCAGATAGTAGTGCTGTCATCATCTGCCTCATCACCATGTTCTTCACCATGCTGGCTCTCATGGCTTCTCTCTATGTCCACATGTTCCTGATGGCCAGGCTTCACATTAAGAGGATTGCTGTCCTCCCC
GGCACTGGTGCCATCCGCCAAGGTGCCAATATGAAGGGAGCGATTACCTTGACCATCCTGATTGGCGTCTTTGTTGTCTGCTGGGCCCCATTCTTCCTCCACTTAATATTCTACATCTCTTGTCCTCAGAATCCATATTGTGTGTGCTTCATGTCTC
ACTTTAACTTGTATCTCATACTGATCATGTGTAATTCAATCATCGATCCTCTGATTTATGCACTCCGGAGTCAAGAACTGAGGAAAACCTTCAAAGAGATCATCTGTTGCTATCCCCTGGGAGGCCTTTGTGACTTGTCTAGCAGATATGGCTCG
AGCGGTGGTGGCGGGAGCGGAGGTGGAGGGTCGTCAGGTGTGACCGGCTACCGGCTGTTCGAGGAGATTCTGTGA

3x HA-MC4R-LgBiT	CMV-β-arrestin1-LgBiT	FW	GTGACTTGTCTAGCAGATATGGCTCGAGCGGTGGTGGCGG	pcDNA3.1-3xHA-MC4R	FW	AACTTAAGCTTGGTACCACCATGTACCCATACGATGTTCC
		RV	GGAACATCGTATGGGTACATGGTGGTACCAAGCTTAAGTTTAAACGCTAGCC		RV	CCGCCACCACCGCTCGAGCCATATCTGCTAGACAAGTCACA

ATGTACCCATACGATGTTCCAGATTACGCTTACCCATACGATGTTCCAGATTACGCTTACCCATACGATGTTCCAGATTACGCTGATGTGAACTCCACCCACCGTGGGATGCACACTTCTCTGCACCTCTGGAACCGCAGCAGTTACAGACTGC
ACAGCAATGCCAGTGAGTCCCTTGGAAAAGGCTACTCTGATGGAGGGTGCTACGAGCAACTTTTTGTCTCTCCTGAGGTGTTTGTGACTCTGGGTGTCATCAGCTTGTTGGAGAATATCTTAGTGATTGTGGCAATAGCCAAGAACAAGAATC
TGCATTCACCCATGTACTTTTTCATCTGCAGCTTGGCTGTGGCTGATATGCTGGTGAGCGTTTCAAATGGATCAGAAACCATTGTCATCACCCTATTAAACAGTACAGATACGGATGCACAGAGTTTCACAGTGAATATTGATAATGTCATTGA
CTCGGTGATCTGTAGCTCCTTGCTTGCATCCATTTGCAGCCTGCTTTCAATTGCAGTGGACAGGTACTTTACTATCTTCTATGCTCTCCAGTACCATAACATTATGACAGTTAAGCGGGTTGGGATCATCATAAGTTGTATCTGGGCAGCTTGCAC
GGTTTCAGGCATTTTGTTCATCATTTACTCAGATAGTAGTGCTGTCATCATCTGCCTCATCACCATGTTCTTCACCATGCTGGCTCTCATGGCTTCTCTCTATGTCCACATGTTCCTGATGGCCAGGCTTCACATTAAGAGGATTGCTGTCCTCCCC
GGCACTGGTGCCATCCGCCAAGGTGCCAATATGAAGGGAGCGATTACCTTGACCATCCTGATTGGCGTCTTTGTTGTCTGCTGGGCCCCATTCTTCCTCCACTTAATATTCTACATCTCTTGTCCTCAGAATCCATATTGTGTGTGCTTCATGTCTC
ACTTTAACTTGTATCTCATACTGATCATGTGTAATTCAATCATCGATCCTCTGATTTATGCACTCCGGAGTCAAGAACTGAGGAAAACCTTCAAAGAGATCATCTGTTGCTATCCCCTGGGAGGCCTTTGTGACTTGTCTAGCAGATATGGCTCG
AGCGGTGGTGGCGGGAGCGGAGGTGGAGGGTCGTCAGGTGTCTTCACACTCGAAGATTTCGTTGGGGACTGGGAACAGACAGCCGCCTACAACCTGGACCAAGTCCTTGAACAGGGAGGTGTGTCCAGTTTGCTGCAGAATCTCGCCGTGT
CCGTAACTCCGATCCAAAGGATTGTCCGGAGCGGTGAAAATGCCCTGAAGATCGACATCCATGTCATCATCCCGTATGAAGGTCTGAGCGCCGACCAAATGGCCCAGATCGAAGAGGTGTTTAAGGTGGTGTACCCTGTGGATGATCATCAC
TTTAAGGTGATCCTGCCCTATGGCACACTGGTAATCGACGGGGTTACGCCGAACATGCTGAACTATTTCGGACGGCCGTATGAAGGCATCGCCGTGTTCGACGGCAAAAAGATCACTGTAACAGGGACCCTGTGGAACGGCAACAAAATTAT
CGACGAGCGCCTGATCACCCCCGACGGCTCCATGCTGTTCCGAGTAACCATCAACAGCTGA

Plasmid name	Backbone	Backbone primers (5’ 3’)		Insert	Insert primers (5’ 3’)	
CMV-SmBiT-β-arrestin 2	pcDNA3.1- ARRB2	FW	GGAGGCTCGAGCGG TATGGGGGAGAAAC CCG	pBiT2.1-N [TK/SmBiT]	FW	GAGCTCGGAT CCACCATG GTGACCGGCT ACC
		RV	GTAGCCGGTCACCA T GGTGGATCCGAGCTC G		RV	GGGTTTCTCC CCCATACC GCTCGAGCCT CC

MVTGYRLFEEILGSSGGGGSGGGGSSGMGEKPGTRVFKKSSPNCKLTVYLGKRDFVDHLDKVDPVDGVVLVDPDYLKDRKVFVTLTCAFR
YGREDLDVLGLSFRKDLFIATYQAFPPVPNPPRPPTRLQDRLLRKLGQHAHPFFFTIPQNLPCSVTLQPGPEDTGKACGVDFEIRAFCAKSLE
EKSHKRNSVRLVIRKVQFAPEKPGPQPSAETTRHFLMSDRSLHLEASLDKELYYHGEPLNVNVHVTNNSTKTVKKIKVSVRQYADICLFSTAQ
YKCPVAQLEQDDQVSPSSTFCKVYTITPLLSDNREKRGLALDGKLKHEDTNLASSTIVKEGANKEVLGILVSYRVKVKLVVSRGGDVSVELPF
VLMHPKPHDHIPLPRPQSAAPETDVPVDTNLIEFDTNYATDDDIVFEDFARLRLKGMKDDDYDDQLC*